R. & M. No. 3492

MINISTRY OF TECHNOLOGY

AERONAUTICAL RESEARCH COUNCIL
REPORTS AND MEMORANDA

Design and Test of a Series of Annular Aerofoils

By D. L. Ryall and I. F. Collins

LONDON: HER MAJESTY'S STATIONERY OFFICE
1967
PRICE £1 2*s.* 6*d.* NET

Design and Test of a Series of Annular Aerofoils

By D. L. Ryall and I. F. Collins

Reports and Memoranda No. 3492
March, 1965

Summary.

The results of a series of wind tunnel tests involving velocity, surface pressure and force measurements on six annular aerofoils are presented together with details of the design procedure which was based on that given by Küchemann and Weber[1]. It is shown that theoretical predictions agreed well with experimental results when the foils were in the design condition, i.e. uniform inflow at zero incidence.

Pressure, lift and drag measurements were also made on the foils at incidence, and the results differed somewhat from predictions of lifting surface theory. Three foils were further tested with concentric centre-bodies and three others in an axisymmetric inflow; in both cases the theoretical predictions agreed well with experimental results.

LIST OF CONTENTS

*Replaces A.R.L./G/R6 — A.R.C. 27 037.

LIST OF APPENDICES

---

1. *Introduction.*

In order to further the progress of another investigation the need arose to design a variety of annular aerofoils which would meet given requirements as to velocity distribution within the foil and minimum pressure on the surface of the foil. A mathematical analysis has long been available, see e.g. Küchemann and Weber[1], for an isolated annular foil placed at zero incidence to a uniform flow. However, at least over the range of annular foil geometry of interest in the present study, there existed no experimental evidence as to the accuracy to which designs would meet their theoretical specification.

It was found necessary therefore to test a number of annular aerofoil designs, in the first instance under the condition of zero incidence to a uniform flow. Since interest in the foils included their behaviour under different flow conditions performance was also measured when a foil was placed at non-zero incidence, when a foil surrounded a parallel-sided centre-body, and when placed at zero incidence to an axi-symmetric shear flow.

2. *Annular Aerofoils at Zero Incidence in Uniform Inflow.*

The mathematical treatment of annular aerofoils developed by Küchemann and Weber[1] and, among others, by Morgan[2] is an extension to the axi-symmetric case of linearized two-dimensional aerofoil theory, *see* for example Thwaites[3]. Since the problem is three-dimensional conformal transformation cannot be used, and the problem has to be linearized to make it tractable. The governing equation of incompressible potential flow (i.e. Laplace's equation) is linear, but the boundary condition on the surface of the aerofoil introduces non-linearities into the problem. This boundary condition, i.e. that the fluid velocity at the aerofoil surface must be parallel to the surface, may be expressed as

$$\text{(radial velocity)/(axial velocity)} = \text{(slope of aerofoil surface)} \tag{1}$$

If V_0 denotes the axial inflow velocity and v_r and v_x the radial and axial components respectively of the perturbation velocity field produced by the annular aerofoil, equation (1) may be written:

$$v_r/(V_0+v_x)\Big|_{\text{surface}} = \frac{d}{dx}\Big[c(x)\pm s(x)\Big] \tag{2}$$

for $0 \leqslant x \leqslant l$, where l is the axial length of the foil, $x = 0$ is the leading edge of the foil and $x = l$ the trailing edge (*see* Fig. 1 for co-ordinate notation), $r = c(x)$ is the equation of the camber line of the foil, and $s(x)$ is the half-thickness distribution of the foil section measured normal to the axis. The upper/lower sign in equation (3) refers to the outer/inner face of the foil.

The foil is assumed to be 'thin' by which is meant

$$\left.\begin{aligned} &c(x)-R_0, \quad s(x)\ll l \\ \text{and} \quad &c'(x), \quad s'(x)\ll 1 \end{aligned}\right\} \tag{3}$$

where R_0 is a mean value of $c(x)$ over the range $0 \leqslant x \leqslant l$. This latter condition cannot be satisfied near a rounded leading edge where $s'(x) \to \infty$, and hence 'thin aerofoil theory' is not realistic near the leading edge of the foil.

The relations (2) and (3) together imply that

$$v_r/(V_0+v_x)\Big|_{\text{surface}} \ll 1$$

Hence, since v_r and v_x are of the same order, the assumption that the annular aerofoil section is 'thin' implies that $v_r,\ \ v_x \ll V_0$. Rewriting (2) in the form:

$$v_r = [c'(x) \pm s'(x)]\, V_0 + [c'(x) \pm s'(x)] v_x \tag{2a}$$

shows that the term involving the axial component of the perturbation velocity is of second order and can be neglected in a linear theory; that is to say the axial component of the perturbation velocity can be neglected in comparison with V_0, the inflow velocity, when applying the boundary condition (1).

Further it is assumed that since the aerofoil section is 'thin' the error in evaluating the velocities on the mean cylinder $r = R_0$ of the foil, rather than on the surface of the foil itself, is also second order.

Thus the final, fully linearized, boundary condition is

$$v_r(x, R_0)/V_0 = c'(x) \pm s'(x) \tag{4}$$

In order to solve Laplace's equation subject to the linear boundary condition (4) the annular foil is replaced by a distribution of source and vortex rings. Theoretically these rings could lie on any single-valued axisymmetric surface lying within the annular aerofoil between the leading and trailing edges, but for ease of calculation the rings are taken as lying on the foil's mean cylinder $r = R_0, \quad 0 \leqslant x \leqslant l$.

The velocity induced on the mean cylinder at the point (x, R_0) by the distribution of source rings of strength density $q(x'), \quad 0 \leqslant x' \leqslant l$, has axial and radial components $v_{qx}(x, R_0)$ and $v^*_{qr}(x, R_0) \pm \frac{1}{2} q(x)$ respectively whilst the induced velocity due to the distribution of vortex rings of strength density $\gamma_0(x'), \quad 0 \leqslant x' \leqslant 1$, has axial and radial components $v^*_{\gamma_0 x}(x, R_0) \mp \frac{1}{2}\gamma(x)$ and $v_{\gamma_0 r}(x, R_0)$ respectively, where the upper/lower sign refers to points on the outer/inner face of the cylinder. The sign convention for the strength of the vortex rings adopted here is that used by Küchemann and Weber[1] and Bagley[4], and is such that $\gamma_0 > 0$ if the vortex ring produces an accelerated flow through the ring itself (*see* Figure 1).

The significance of the asterisk in the above notation is to emphasize that v^*_{qr} and $v^*_{\gamma_0 x}$ are only the regular part of the velocities induced on the mean cylinder of the foil, the radial component of the source-ring distribution having discountinuity of $q(x)$ and the axial component of the vortex-ring distribution a discontinuity of $-\gamma_0(x)$ across the mean cylinder of the foil.

Analytic expressions for these four velocity components are given in Appendix I in terms of Bessel functions, elliptic integrals and Legendre functions of the second kind and half order.

Substituting for $v_r(x, R_0)$ in the linearized boundary condition (4):

$$v^*_{qr}(x, R_0) \pm \tfrac{1}{2} q(x) + v_{\gamma_0 r}(x, R_0) = V_0 [c'(x) \pm s'(x)] \tag{5}$$

where the upper/lower sign refers to the outer/inner face as before. Separating the two parts of equation (5):

$$q(x) = 2 V_0 s'(x) \tag{6}$$

and

$$v^*_{qr}(x, R_0) + v_{\gamma_0 r}(x, R_0) = V_0 c'(x). \tag{7}$$

Thus the strength of the source-ring distribution and the thickness distribution are related by the simple expression (6) (which is the same expression found in two-dimensional aerofoil theory—Thwaites[3]) and if either $q(x)$ or $s(x)$ is known the other is easily calculated.

The relation between the camber gradient and the vortex distribution is more complicated. Two distinct problems are evident:

(a) A design procedure in which $\gamma_0(x)$ is determined from some requirement on the velocity field of the annular foil; in the designs presented in this report the foil is desired to produce a specified mean velocity increment in its mid-plane. The thickness distribution $s(x)$ and the chord-diameter λ are also specified, and the problem is to calculate the camber line of the foil. This is readily done using equation (7); $q(x)$ is known from (6) and v^*_{qr} and $v_{\gamma_0 r}$ can be evaluated using the expressions given in Appendix I, e.g. in terms of elliptic integrals:

$$v^*_{qr}(x, R_0) = \frac{1}{2\pi R_0}\int_0^l q(x')\left[\tfrac{1}{2}k^3 D(k)\right] dx' \qquad \text{I.28}$$

$$v_{\gamma_0 r}(x, R_0) = \frac{1}{2\pi R_0}\int_0^l \gamma_0(x')\left[k' k^2 D(k) - k E(k)\right] dx' \qquad \text{I.29}$$

where
$$k^2 = 4\Big/\left[\left(\frac{x-x'}{R_0}\right)^2 + 4\right] \text{ and } k'^2 = 1-k^2. \qquad \text{I.30}$$

(b) Secondly, there is the inverse problem of calculating the source and vortex distributions and hence the velocity field of a given annular foil. The strength of the source distribution $q(x)$ is readily calculated from (6) but, as can be seen from the expression I.29 for $v_{\gamma_0 r}(x, R_0)$, equation (7) is now an integral equation for $\gamma_0(x)$. Hence this second problem is far more complicated than the straight-forward design procedure. This report is only concerned with the first type of problem; the inverse problem is dealt with by Morgan[2] and in a series of reports published by Therm Advanced Research.[5,6,7,8]

It is of interest to note that the presence of the term v^*_{qr} in equation (7) is an additional complication due to the three-dimensional nature of the aerofoil and is not present in the corresponding two-dimensional theory. Thus for an uncambered annular aerofoil (i.e. $c'(x) = 0$), the vortex distribution is not identically zero and there is a net circulation around each section of the foil.

As is described in the next Section two series of foils were designed and tested, the first series being designed in accordance with the linear theory so far presented, but in the design of the second series it was felt necessary to take some account of the axial component of the perturbation velocity in applying the boundary condition (2) since, for instance, for the foil B.1. $v_x/V_0 \sim 0{\cdot}3$ (*see* later for details of foils). The design method for the second series of foils thus incorporated a non-linear modification used by Küchemann and Weber[1] and Bagley[4] which is described below.

In the design problem $q(x)$ and $\gamma_0(x)$ are both known so that v_{qx} and $v^*_{\gamma_0 x}$ can be calculated and hence these terms can be included in the axial velocity in equation (7) when evaluating $c'(x)$, i.e.

$$v^*_{qr}(x, R_0) + v_{\gamma_0 r}(x, R_0) = \left[V_0 + v_{qx}(x, R_0) + v^*_{\gamma_0 x}(x, R_0)\right] c'(x). \qquad (8)$$

However two comments must be made regarding the application of (8) to an aerofoil with non-zero thickness:

(a) The error in evaluating the velocities on the mean cylinder rather than on the foil surface is also a second order quantity, and so the above correction only goes half way towards a second order theory.

(b) To be consistent the $\mp\frac{1}{2}\gamma_0(x)$ term should be included in the axial velocity in equation (5), and also the v_{qx}, $v^*_{\gamma_0 x}$ terms in equation (6). Equations (6) and (7) should now be replaced by

$$\left(V_0 + v_{qx} + v^*_{\gamma_0 x}\right) s'(x) - \tfrac{1}{2}\gamma_0(x)\, c'(x) = \tfrac{1}{2} q(x) \qquad (9)$$

and

$$(V_0+v_{qx}+v^*_{\gamma_0 x})\,c'(x)-\tfrac{1}{2}\gamma_0(x)\,s'(x) = v^*_{qr}+v_{\gamma_0 r}. \tag{10}$$

Eliminating $c'(x)$ from these two equations we have a non-linear integral equation for $q(x)$, necessitating a great deal of computation for only a small gain in accuracy.

In view of these theoretical objections to the use of equation (8) in the design procedure its justification must rely upon experimental results.

The foil having been designed for a given circulation distribution it is of interest to calculate the theoretical pressure distribution on its surface or, conversely, an empirical circulation distribution may be deduced from measurements of the pressure on the surface of the foil.

The pressure coefficient C_p is defined by

$$C_p = (p-p_0)/\tfrac{1}{2}\rho {V_0}^2 \tag{11}$$

where p_0 is the static pressure and V_0 the velocity of the free stream. Using Bernoulli's Theorem for irrotational flow, C_p can also be expressed as

$$C_p = 1-[(V_0+v_x)^2+{v_r}^2]/{V_0}^2 \tag{12}$$

where v_r, v_x are the radial and axial components of the perturbation velocity of the foil.

In the linear theory both v_r and v_x are assumed small in comparison with V_0, and thus to a first order

$$C_p = -2\,v_x/V_0. \tag{13}$$

In the non-linear modification however v_x is not necessarily small compared with V_0, and so to a first order

$$C_p = -2\,v_x/V_0-(v_x/V_0)^2. \tag{14}$$

C_p can be evaluated on the aerofoil surface using either (13) or (14), whichever is appropriate, since in either case

$$v_x(x, R_0) = v_{qx}(x, R_0)+v^*_{\gamma_0 x}(x, R_0)\mp\tfrac{1}{2}\gamma_0(x) \tag{15}$$

where the upper/lower sign refers to the outer/inner face as usual.

On the other hand using equations (13) and (15) a simple expression can be obtained for the circulation distribution $\gamma_0(x)$, in terms of the pressure coefficients on the outer and inner faces. If $(C_p)^+$, $(C_p)^-$ denote the pressure coefficients on the outer, inner faces respectively, then

$$(C_p)\pm = -2\,[v_{qx}+v^*_{\gamma_0 x}\mp\tfrac{1}{2}\gamma_0(x)]/V_0$$

and therefore

$$(C_p)^+-(C_p)^- = +2\gamma_0(x)/V_0. \tag{16}$$

3. *The Design of the Annular Aerofoils.*

The procedure used in the design of the six foils tested in these experiments is outlined here, whilst the geometric details of the individual foils are given in the next Section.

In each case the chord-diameter ratio ($\lambda = l/2R_0$) was specified together with the section thickness distribution $s(x)$, and $q(x)$ calculated from (6). Further the vortex distribution $\gamma_0(x)$ was chosen to be constant along the length of the chord (*c.f.* NACA $a = 1$ type camber lines for two-dimensional aerofoil sections). i.e.

$$\gamma_0(x) = 2\pi V_0 b \tag{17}$$

where b is a constant. This vortex distribution is essentially the fourth term of the Birnbaum Series employed by Küchemann and Weber[1], and the induced velocities associated with such a vortex distribution are tabulated in the Appendix of Ref. 1 for various chord/diameter ratios. The analytic expressions involved are given here in Appendix I.

Each foil was designed to have a particular 'diffusion ratio' Δ defined as the ratio of the mean velocity inside the foil across the mid-chord plane of the foil to the uniform inflow velocity V_0.

This diffusion ratio is related to $q(x)$ and $V_0(x)$ by the equation

$$\Delta V_0 = V_0 + \bar{v}_q + \bar{v}_{\gamma_0} \tag{18}$$

where $\bar{v}_q$ and $\bar{v}_{\gamma_0}$ are the mean velocities in the mid-chord plane produced by the source and vortex distributions respectively. $\bar{v}_q$ can be evaluated by numerical integration, and for the constant vortex distribution chosen for these designs $\bar{v}_{\gamma_0}$ can be evaluated analytically as is shown in Appendix I since

$$\bar{v}_{\gamma_0} = 8\, k_3' \, D(k_3)\, V_0\, b \tag{I.26}$$

where

$$k_3 = +\sqrt{\frac{4}{(l/2R)^2+4}} = +\sqrt{\frac{4}{\lambda^2+4}}, \quad k_3' = +\sqrt{1-k_3^2} \tag{I.27}$$

and $D(k)$ is the complete elliptic integral of the third kind.

A given diffusion ratio thus determines the value of b and the consequent circulation around a section of the foil. However in calculating the required camber line *via* equation (7) some allowance needs to be made for real fluid effects. It is known that for a two-dimensional aerfoil with an $a = 1$ type camber line the lift, and hence the total circulation, is only 74 per cent of that predicted by inviscid flow theory. This is due to the displacement thicknesses of the boundary layers on the two faces being different, owing to the different pressure distributions, which results in a change in the effective camber of the aerofoil. It is not known to what extent the curvature of flow in the three-dimensional case of the annular aerofoil will affect the boundary-layer development compared to that in the two-dimensional case and, in particular, it is not clear how the 'inviscid' chordwise distribution of circulation will be altered by the presence of viscosity. It has therefore been assumed for design purposes that real fluid effects reduce the vortex strength uniformly to 0·74 of that predicted from inviscid flow theory. Thus in calculating $c'(x)$ from equation (7) the contribution from the vortex distribution term was scaled up by a factor $\frac{1}{0{\cdot}74} = 1{\cdot}35$.

Thus once b has been determined, $v_{\gamma_{0r}}$ and $v^*_{\gamma_{0x}}$ can be calculated from the expressions given in Appendix I, or read off from Tables in the Appendix of Reference 1, at various stations along the mean cylinder of the foil. $c'(x)$ is then calculated using equation (7) (or (8) if the non-linear theory is employed) and scaling up the contribution from the vortex distribution term by the factor $\frac{1}{0{\cdot}74} = 1{\cdot}35$. (In the present designs

twenty equally spaced stations were used.) The camber line $c(x)$ can then be evaluated by numerical integration, the constant of integration being chosen such that R_0 is some mean value of $c(x)$ in $0 \leqslant x \leqslant l$. (In the present designs the arithmetic mean was taken.)

4. *Particular Designs Tested.*

Two sets of annular foils were designed and tested in these experiments. The mean diameter was chosen to be 12 ins. and the section thickness distribution was chosen in all cases to be the NACA 0006 section, slightly thickened at the trailing edge for structural reasons.

The three foils of Set A, which were turned out of laminated wood, each had a chord/diameter ratio of unity, the design diffusion ratio (i.e. the mean velocity across the mid-plane relative to the free stream) being 0·63, 0·82 and 1·00 respectively. They were designed on the basis of the fully linearized theory using equations (6) and (7) to determine the camber line.

An estimate was later made of the performance of these foils according to the non-linear theory, i.e. using equations (6) and (8). This involved solving the inverse problem of calculating the velocity field of a given annular foil. The iteration procedure developed at Therm[6] was used to solve the basic integral equation and a second interative procedure was adopted to deal with the non-linear term $(v_{qx}+v^*_{70x})$ of equation (8). This calculation is not as precise as that using equations (6) and (8) in a design procedure as allowance has to be made for real fluid effects. Since the resulting circulation (inviscid theory) is no longer rectangular the appropriate viscous correction may well be different from that assumed (0·74, as for rectangular distribution). The resulting estimates of the diffusion ratios of the three foils were 0·70, 0·84 and 1·00 respectively.

The three foils of Set B each have a chord/diameter ratio of 0·75, their design diffusion ratios being 0·73, 0·91 and 1·19 respectively. This set was designed on the basis of the non-linear theory using equations (6) and (8) to determine the camber line. These foils were cast and machined from Araldite incorporating pressure tubes with holes in both inner and outer faces, at positions 5, 10, 20, 30, 40, 50, 70 and 85 per cent of the chord, measured from the leading edge. There were two sets of these holes, one set lying on a line parallel with the axis of the foil, the other on a line inclined at 30 deg to the axial direction. This enabled any interference between the pressure holes of the former set which lie on a streamline, to be determined by comparison with the latter.

Photographs of one foil from each set are shown in Figures 3 and 4 respectively, and the design ordinates of the surfaces of all six foils are tabulated in Appendix II.

5. *Experimental Results for Annular Aerofoils under Design Flow Conditions.*

All the experiments described in this report were carried out in one of the N.P.L. low speed 9 ft × 7 ft wind tunnels with a working section of length 12 ft.

All six foils were first tested in a uniform stream and at zero incidence. Photographs of one of the foils rigged in the wind tunnel are shown in Figures 5 and 6. Measurements were made at two free-stream velocities—100ft/sec and 180 ft/sec. Velocity traverses, using a five-hole probe, were made across the mid-chord plane and across the trailing edge plane of each foil and results for the lower speed are shown in Figures 12, 13 and 14. Theoretical velocity distributions are shown for the mid-chord plane based on the linear design method for Set A and the non-linear procedure for Set B.

The mean velocities $\overline{V}/V_0$ across the mid plane of the foils are tabulated below:

TABLE 1

Annular Foil at Zero Incidence
Ratio of Mean Mid-Plane Velocity $\bar{V}$ to Inflow Velocity V_0
(i.e. Diffusion Ratio)

	Set A $\lambda = 1{\cdot}00$			Set B $\lambda = 0{\cdot}75$		
	1	2	3	1	2	3
Theoretical { Linear	0·63	0·82	1·00	—	—	—
predictions { Non linear	0·70*	0·84*	1·00*	0·73	0·91	1·19
Experimental	0·68	0·81	1·00	0·74	0·91	1·24

*N.B.—The non-linear predictions for Set A were estimated after the foils had been designed according to the linear analysis, as is explained in Section 4.

Agreement between the non-linear predictions and the experimental values of the velocity distribution across the mid-chord plane and its mean value is good in all cases except for the only accelerating foil B.3. It will be noted in particular that the non-linear estimate of $\bar{V}/V_0$ for the foil A.1 is a marked improvement on the linearized design figure. The cause of the discrepancy between predicted and experimental values for B.3 is not clear. It is suggested that it may be due, in part at least, to the speeding up of the flow through the foil caused by the presence of the thick boundary layer on the suction face of the foil, which for an 'accelerating' foil is the inner face.

The measured pressure distributions for the foils of Set B are shown in Figure 15 together with theoretical curves derived from equation (14) based on the non-linear theory. Agreement is seen to be good except for the first 20 per cent of the pressure face where the theory is known to be invalid, and on the inner (suction) face of foil B.3 where the theory underestimates the suction.

From the measured pressure distributions empirical circulation distributions can be deduced using equation (16) (which is based on the linear theory); these are shown in comparison with the uniform theoretical distribution in Figure 16. Improved values of the empirical circulation distribution are also shown in Figure 16; these were derived through the use of equation (14) of the non-linear analysis. It is now no longer possible to eliminate v_{qx} and $v_{\gamma_0 x}$ from the equation for $\gamma_0(x)$ and hence the theoretical values (suitably corrected for viscosity) were used in deriving this second approximation to the empirical circulation distribution.

As expected, due to the inadequacies of thin aerofoil theory near the leading edge and to the effects of the boundary layers, the uniform circulation distribution is not obtained, although the total circulation for each of the two diffusing foils B.1 and F.2 agrees well with the predicted value. This endorses the conclusion deduced from the velocity measurements that 0·74 is an appropriate viscous correction factor for these two foils. The estimated total circulation for the third foil does not agree well with the predicted value but is in agreement with the experimental velocity measurements, showing that the pressure and velocity measurements for foil B.3 are consistent, as they are for the other foils of Set B.

As stated above, both velocity traverses and pressure measurements were made at two speeds, 100 ft/sec and 180 ft/sec, but no significant Reynolds' number effect was found in this range. These measurements were also made with trip wires attached on both the inner and outer faces of the foils at 0·25 ins. from the leading edge, but no significant change was found in the readings.

6. *Theoretical Predictions for Annular Aerofoils at Incidence.*

A linearized, lifting surface theory for annular aerofoils at small incidences in a uniform inflow has been developed by Weissinger[9], Bagley et al[4] and Morgan[2].

The notation is shown in Figure 2, (r, θ, x) being right-handed cylinderical co-ordinates, with x axis coincident with the axis of the annular foil, and origin in the leading-edge plane of the foil. The reference radial line $\theta = 0$ is chosen such that the inflow velocity V_0 has components $V_0 \cos\alpha$ in the axial direction and $V_0 \sin\alpha \cos\theta$ in the radial direction, α being the angle of incidence of the foil.

As in the case of an annular foil at zero incidence, the foil can be represented by a system of bound ring sources and vortices on the foil mean cylinder ($r = R_0$, $0 \leqslant x \leqslant 1$), where the strength of the vortices now depends on θ as well as on x. But in addition since the strength of the bound ring vortices has an angular variation there exist bound and trailing axial vortices, their axes being assumed to lie on the semi-infinite cylinder $r = R_0, x \geqslant 0$. This assumption restricts the validity of the theory to small angles of incidence.

The same two linearizing approximations made in the case of the foil at zero incidence are also made here. That is to say the axial component of the perturbation velocity produced by the foil is neglected in comparison with $V_0 \cos\alpha$ the axial component of the inflow velocity, and in stating the boundary condition the velocity components are evaluated on the mean cylinder of the foil instead of on the aerofoil surface. Equation (5) will however be modified for the foil at incidence by the addition of two extra components of radial velocity:

(a) $V_0\alpha \cos\theta$—the radial component of the inflow velocity and

(b) $v_{\gamma_2 r}(\theta, x)$—the radial component of the velocity induced by the axial vortex system, with strength

$$\left.\begin{aligned} \gamma_2 \equiv \gamma_2(\theta, x') &= -\int_0^{x'} \frac{\partial\gamma}{\partial\theta}\, dx'' \quad 0 \leqslant x' \leqslant l \\ \equiv \gamma_2(\theta) \quad &= -\int_0^{1} \frac{\partial\gamma}{\partial\theta}\, dx'' \quad l \leqslant x' \end{aligned}\right\} \tag{19}$$

where $\gamma = \gamma(\theta, x')$ is the strength of the bound vortex-ring system.

The linearized boundary condition is

$$V_0[c'(x) \pm s'(x)] = v^*_{qr}(x) \pm \tfrac{1}{2} q(x) + v_{\gamma r}(\theta, x) + v_{\gamma_2 r}(\theta, x) + V_0\alpha \cos\theta. \tag{20}$$

Thus
$$q(x) = 2 V_0 s'(x) \tag{21}$$

and
$$V_0 c'(x) = v^*_{qr}(x) + v_{\gamma r}(\theta, x) + v_{\gamma_2 r}(\theta, x) + V_0\alpha \cos\theta. \tag{22}$$

The problem is to calculate the pressure and velocity fields of a given foil, $c(x)$, $s(x)$ being known, at a given incidence α. Equations (21) and (22) are to be regarded therefore as equations for $q(x)$ and $\gamma(\theta, x)$.

As equation (21) is identical with equation (6) the source distribution $q(x)$ is seen to be independent of incidence and of θ, depending only on the section thickness distribution. The vortex distribution given by the integral equation (22) depends however both on incidence α and on θ. Consider $\gamma(\theta, x')$ to be the sum of two separate vortex distributions: $\gamma_0(x')$ the ring-vortex distribution at zero incidence given by equation (7), and $\gamma_1(\theta, x')$ the additional bound-ring vorticity due to incidence. Then the strength of the axial vorticity is given by

$$\left.\begin{aligned} \gamma_2(\theta, x') &= -\int_0^{x'} \frac{\partial\gamma}{\partial\theta}\, dx'' = -\int_0^{x'} \frac{\partial\gamma_1}{\partial\theta}\, dx'' \qquad 0 \leqslant x' \leqslant l \\ &= -\int_0^{l} \frac{\partial\gamma}{\partial\theta}\, dx'' = -\int_0^{l} \frac{\partial\gamma_1}{\partial\theta}\, dx'' \qquad l \leqslant x' \end{aligned}\right\} \tag{23}$$

and thus depends only on the additional ring vorticity γ_1.

Eliminating $c'(x)$ from (7) and (22) the following equation is obtained for $\gamma_1(\theta, x')$:

$$v_{\gamma_1 r}(\theta, x)+v_{\gamma_2 r}(\theta, x)+V_0\alpha\cos\theta = 0. \tag{24}$$

Since this equation does not involve $q(x')$, $\gamma_0(x')$, $s'(x)$ or $c'(x)$, the strength $\gamma_1(\theta,x')$ is independent of the section thickness distribution and camber and depends only on the chord/diameter ratio λ.

The singular integral equation (24) can be solved by expanding $\gamma_1(\theta, x')$ as a Fourier series in θ and a Glauert series in ϕ (or equivalently a Birnbaum series in x') where ϕ is the conventional eccentric angle of thin aerofoil theory given by

$$x' = \tfrac{1}{2}\, l\,(1-\cos\phi). \tag{25}$$

As can be seen from equation (24), the only dependence of $\gamma_1(\theta, x')$ on θ is through $\cos\theta$, and hence the only non-zero coefficient in the Fourier expansion of $\gamma_1(\theta, x')$ in θ is that of $\cos\theta$; therefore

$$\gamma_1(\theta, x') = V_0\alpha\cos\theta f(x'). \tag{26}$$

Then $f(x') \equiv f(\phi)$ is expanded in a Glauert expansion:

$$f(\phi) = 2\pi\,(K_0\cot\tfrac{1}{2}\phi+\sum_1^\infty K_n\sin n\,\phi). \tag{27}$$

The insertion of (26) and (27) into (24) leads to the determination of the coefficients K_0, K_1, etc. (*see*, for example, Morgan [2]) which depend only on the chord/diameter ratio; they are tabulated for various λ in Ref. 4†.

Using the Kutta-Joukowsky condition an expression for the lift on the annular foil in terms of the coefficients K_0, K_1 etc., can readily be deduced. Thus the lift on the foil is given by

$$L = -\rho V_0\int_0^l\int_0^{2\pi}\gamma(\theta,x')\cos\theta\, R_0\, d\theta\, dx'.$$

Substituting for $\gamma(\theta, x')$ from (26) and (27)

$$L = -\rho V_0^2\alpha\, 2\pi\int_0^{2\pi}\cos^2\theta R_0 d\theta\int_0^{\pi}(K_0\cot\tfrac{1}{2}\phi+\sum_1^\infty K_n\sin n\,\phi)\sin\phi\,(\tfrac{1}{2}\, l\, d\,\phi).$$

Carrying out the integrations with reference to θ and ϕ

$$L = -\tfrac{1}{2}\rho V_0^2(2\, R_0\, l\,)\alpha\,\pi^3\,(K_0+\tfrac{1}{2}\,K_1).$$

Defining the lift coefficient C_L by

$$C_L = \frac{L}{\tfrac{1}{2}\rho V_0^2\,(2\, R_0\, l)}$$

this gives

$$C_L = -\pi^3\,(K_0+\tfrac{1}{2}K_1)\alpha. \tag{28}$$

---

† (Footnote:) $K_0 = A_1/\tan\alpha$,—$K_1 = A_2/\tan\alpha$,—$K_2 = 2A_3/\tan\alpha$.... where A_1, A_2 etc. are the coefficients in the Birnbaum expansion used in Ref. 4.

For $\lambda = 0{\cdot}75$, this expression gives a value of 0·063 for the lift slope $\partial C_L/\partial\alpha$ where α is in degrees. For a two-dimensional foil with an NACA 0006 section the experimental lift slope is very close to the theoretical value at small incidences, and so no corrections for thickness seemed necessary for the annular foils considered here.

An expression for the induced drag coefficient of an annular foil is given by Weissinger[9] and Fletcher[10]:

$$C_{D_i} = C_L{}^2/2\pi A \tag{29}$$

where $A = 2R_0/l = 1/\lambda$ is the 'aspect ratio' of the foil. This is equivalent to assuming that the induced drag of the foil is one half the induced drag of a rectilinear wing with the same aspect ratio and with elliptic loading. For $\lambda = 0{\cdot}75$, equation (29) gives $C_{D_i} = 0{\cdot}119\,C_L{}^2$ and, by using the value of $\partial C_L/\partial\alpha$ predicted from (28), it is predicted that $C_{D_i} = 0{\cdot}00047\alpha^2$ where α is in degrees.

7. Experimental Results with Annular Aerofoils at Incidence.

The three foils of Set B were mounted on a short strut via a swivel coupling, for varying the incidence, onto the strut of an aerodynamic balance so that lift and drag measurements could be made. A photograph of one of the foils so mounted is shown in Figure 7. Pressure distributions were measured using the set of pressure holes lying in the half-plane $\theta = 0$ (*see* Figure 2 for notation).

Tare corrections to the lift and drag measurements to allow for the support strut and the two inches of hyperdermic tubing trailing behind the foil were found by using a dummy strut and a dummy set of tubes. A correction was made to the drag to cancel out the drag of the trip wires where these were employed. This correction was found by measuring the drag of the foil with trip wires of five different diameters each being large enough to trip the laminar boundary layer. The drag against trip wire diameter curve was then extrapolated to zero wire diameter to find the true drag of the foil with fully turbulent boundary layers.

The lift, drag and pressure distributions were taken at two speeds, 100 ft/sec and 180 ft/sec, and over a range of incidence from -10 deg to $+10$ deg at intervals of 2·5 deg. Repeat settings showed this incidence was set accurately to within $\pm 0{\cdot}1$ deg.

The lift coefficient against incidence curves are plotted in Figure 17. The values of the mean lift slopes between -5 deg and $+5$ deg are tabulated below.

TABLE 2

Annular Foils at Incidence
Measured Values of Mean Lift Slopes

	Foil B.1.	Foil B.2.	Foil B.3.
Measured diffusion ratio	0·74	0·91	1·24
$\partial C_L/\partial\alpha$ 100 ft/sec	0·054 ± 0·001	0·059 ± 0·001	0·064 ± 0·001
$\partial C_L/\partial\alpha$ 180 ft/sec	0·053 ± 0·001	0·059 ± 0·001	0·064 ± 0·001

These results show generally a deviation from the value predicted by inviscid flow theory, *viz.* 0·063, and a significant variation of the lift slope with camber. It is suggested that this difference from inviscid theory may be attributable to the adverse pressure gradients which are greater than in the two-dimensional case. The gradients differ between the foils which therefore develop different boundary layer characteristics and hence the 'real fluid' correction to the lift slope varies.

A further feature of the lift-incidence curves in Figure 17 is the S-shape, with the slope increasing with increasing incidence; this is most noticeable for the highly diffusing foil B.1. This type of curve is a well-known feature of solid axisymmetric bodies at incidence, where it is due to cross flows occurring in the boundary layer producing a larger lift than expected from predictions based on inviscid theories—*see*, for example, Allen[11]. In the present case, however, it is thought more likely that this S-shape arises from the separation of the flow near the leading edge of the foil on one or other surface. For instance in the case of the diffusing foil B.1 this separation occurs on the inner surface behind the point A in Figure 2 for large negative incidences. This was demonstrated directly by attaching woollen tufts near the leading edge. The sample pressure distributions in Figure 19 show a loss in lift near the leading edge on the suction face but a gain in lift over the remaining part of the section producing an overall gain in lift. The presence of separation is not surprising when it is appreciated that for the diffusion ratios achieved here the section lift coefficients are large; it is 0·9 for the foil B.1 with measured $\Delta = 0{\cdot}74$.

Tripping the boundary layer was found to have no significant effect on the values of C_L.

The results of the drag measurements are shown in Figure 18 in the form of lift-drag polars. The results shown are those obtained when both boundary layers were fully turbulent.

The total drag coefficient C_D is given by

$$C_D = C_{D_0} + C_{D_i} \tag{30}$$

where C_{D_0} is the profile drag and C_{D_i} the induced drag due to lift. Equation (29) was used to predict a value for C_{D_i}, but since it was found above that the measured lift coefficient differed appreciably from that predicted by lifting-surface theory, the measured rather than the theoretical value of C_L was inserted into the expression for C_{D_i}. The predicted curves shown in Figure 18 were thus obtained taking the experimental value of the drag at zero lift and assuming that the profile drag does not vary with incidence.

As can be seen from Figure 18, there is a wide discrepancy between measured and predicted values of C_D which increases with C_L, particularly for foil B.1. If it is assumed that C_{D_i} is given adequately by equation (29), this discrepancy must be put down to the variation of profile drag with incidence; the values of profile drag obtained from $C_{D_0} = C_D - C_L^2/2\pi A$ are tabulated in Table 3.

TABLE 3

Annular Foils at Incidence

Variation of Profile Drag

	Foil B.1		Foil B.2		Foil B.3	
Design diffusion ratio	0·74		0·91		1·24	
Velocity (ft/sec)	100	180	100	180	100	180
Incidence (deg)	Profile drag coefficient					
0	0·056	0·050	0·045	0·041	0·050	0·045
5	0·065	0·061	0·045	0·040	0·049	0·045
10	0·097	0·091	0·069	0·057	0·064	0·055

For a two-dimensional foil the profile drag remains constant over a limited range of incidence and then increases fairly sharply as the separation point moves up the suction face of the foil from the trailing edge. In the present case reference to Figure 18 and Table 3 shows that the profile drag remains constant over a range of incidence of $\pm 2{\cdot}5$ deg for foil B.1 and of ± 5 deg for foils B.2 and B.3, but increases as the incidence increases outside these limited ranges. In addition, at the higher incidences separation occurred near the leading edge on the suction face as was mentioned in the discussion of the results of lift, this leading-edge separation having the effect of accentuating the increase in profile drag at the higher incidences.

Apart from changing the value of the profile drag at zero incidence, the trip wire was found to have no significant effect on the drag.

The pressure distributions on the foils at incidence are tabulated in Appendix 3. It was found that the only effect of the trip wire on the pressure readings was to give a spurious value at the first pressure point at $x/l = 0{\cdot}05$ immediately behind the trip wire. The results quoted are therefore those with no trip wire present.

These readings again indicate that the boundary layer separates near the leading edge on the inner face near A (*see* Figure 2) at large negative incidences for decelerating foils B.1 and B.2 and on the outer face near A at large positive incidences for the accelerating foil B.3. The peak suction is found to drop suddenly as the incidence is increased beyond a certain critical angle, producing the decrease of lift in this region referred to earlier.

From these pressure readings it is possible to deduce values for the circulation distribution using equation (16), which must also apply to an annular foil at incidence where the vortex distribution γ now depends on θ as well as on x. Further, assuming $\gamma_1(\theta, x)$ varies as $\cos\theta$ and is proportional to α, we can calculate empirical values for the function $f(x')$ using equation (26). Figure 20 shows points obtained by taking the average value of $f(x')$ calculated from the loadings at $+5$ deg and -5 deg in comparison with the theoretical curve. The overall agreement is seen to be reasonably good.

It is therefore concluded that the lifting surface theory predicts the behaviour of these annular foils at incidence fairly well. However, camber (and hence diffusion ratio) of the foils has a significant effect on the value of the lift coefficient, even at low incidence. The theory also breaks down at the higher incidences due to separation near the leading edge, accompanied by eddy shedding, reducing the value of the peak suction but increasing the lift and drag.

8. *Annular Foils with a Concentric Centre-Body.*

It was of interest to investigate the effect of a centre-body on the performance of an annular foil positioned at either the upstream end of the body where the flow is more or less uniform or towards its downstream end where a boundary-layer shear flow has been generated. In the latter case it is useful to separate the displacement effect of the centre-body itself and the effect of the shear flow of a large boundary layer. The first experiment to be described here is one with the foils mounted well forward on a centre-body while the second experiment to be described in the following Section had the foils mounted in the wake downstream of a large streamlined body to minimize potential flow body-foil interaction.

The exact solution of the potential flow past an annular aerofoil with centre-body is very complicated, and so a much simplified mathematical analysis was used to derive a theoretical estimate of the change in diffusion ratio caused by the presence of the centre-body.

The annular foil was represented by a single vortex ring and the centre-body by a distribution of vortex rings of finite length lying on a cylinder of the same radius r_c. This vortex distribution was regarded as being a linear sum of the first five terms of the Birnbaum series (*see* e.g. Ref. 1); by consideration of symmetry only the coefficients of the second and fourth terms are non-zero. The length of the vortex distribution was chosen so that the maximum/minimum values of the radial velocity induced on the cylinder $r = r_c$ by the vortex ring (representing the foil) coincide with the ends of the finite vortex-ring distribution and hence with the maximum/minimum values of the radial velocity induced by the vortex distribution. The coefficients of the two non-zero terms in the Birnbaum expansion were then deduced by applying the boundary condition, i.e. the total radial velocity is zero, at two axial stations on the cylinder $r = r_c$.

The change in diffusion ratio was then calculated from the stream function of the vortex distribution on the cylinder $r = r_c$ for two diameter ratios. This additional increment is tabulated below:

TABLE 4

Estimate of Velocity Increment due to Centre-Body

Foil / Radius of centre-body	A1	A2	A3
(1/3) R_0	−0·01	−0·01	0·00
(1/2) R_0	−0·04	−0·02	0·00

These increments are seen to be small so that no justification arose for a more complicated analysis of body/aerofoil interaction.

The three foils of Set A were tested with two wooden centre-bodies, both 6 ft long, with parallel sided centre sections of diameter 4 in. and 6 in. respectively, having 2:1 elliptic noses and conical tails. Hence (body diameter)/(foil diameter) ratios were 1:3 and 1:2 respectively. A sketch of the geometry is shown in Figure 8 and a photograph of a foil and centre-body rigged in position in Figure 9. The foils were mounted with the leading edge one foil chord-length back from the beginning of the parallel section of the centre-body, as is shown in Figure 8, so that the thickness of the boundary layer on the centre-body is small in comparison with the foil diameter and can be neglected.

Velocity measurements were made in the mid-chord plane and trailing edge plane of each foil, and these are shown in Figures 21, 22 and 23. The mean velocities in the mid-chord plane for the three foils are tabulated below together with those obtained with no centre-body (*see* Section 5).

TABLE 5

Annular Foil with Centre-Body

Mean Velocity in Mid-Chord Plane $\overline{V}/V_0$

Foil / Radius of centre-body	A1	A2	A3
0	0·68	0·81	1·00
(1/3) R_0	0·66	0·80	1·00
(1/2) R_0	0·65	0·79	1·00

These measurements were made at two speeds 100 ft/sec and 180 ft/sec but no significant Reynolds Number effect was found.

It can be seen from the Tables above that the effect of the centre-body is to reduce even further the mean velocity through the mid-plane of the decelerating foils A1 and A2. The measured magnitude of the influence of a centre-body is in good agreement with the theoretical estimates.

It is concluded that the centre-bodies of interest here have only a small effect on the mean velocity in the mid-chord plane of an annular aerofoil where the centre-body does not exceed half the diameter of the foil. An adequate estimate of the effect of the centre-body can be obtained from an approximate calculation and the large amount of extra computation necessary for an accurate solution is not justified.

Surface pressure distributions were not measured in this series of tests but it is reasonable to assume that these would have been little affected by the presence of either centre-body.

9. *Theoretical Predictions for Annular Aerofoils in an Axisymmetric Shear Flow.*

As was mentioned in the previous Section, it was of interest to study the behaviour of annular foils when the inflow is no longer uniform but has a radial variation as in an axisymmetric boundary layer or wake.

The general solution to the problem of an annular aerofoil in an axisymmetric shear flow is very complicated and has not been attempted here.

As a first approximation to calculating the mean velocity across the mid-chord plane of the foil the rotational nature of the inflow is ignored. The foil is then assumed to produce the same non-dimensional velocity increment (or decrement), i.e. $(\Delta-1)$, as it does when in a uniform stream with velocity equal to $V_w(R_0)$, the velocity of the shear inflow at the foil's mean radius R_0. If $\overline{V}_w$ is the average velocity of the shear inflow over the disc $r = R_0$, then the mean velocity in the mid-plane of the foil will be

$$\overline{V} = \overline{V}_w + (\Delta - 1)\, V_w(R_0). \tag{31}$$

Equation (31) was used to predict values of $\overline{V}$ for the three foils of Set B using the experimental values of Δ for the uniform flow case and these are tabulated in Table 6.

In addition to the simple, probably dominant, effect discussed above, three distinct secondary effects were considered. The corresponding increments to $\overline{V}$ due to these effects are also shown in Table 6 together with the resultant estimate of $\overline{V}$.

(a) Firstly, due to the accelerating (or decelerating) action of the foil, the inflow velocity on the streamline which stagnates on the leading edge of the foil will not be $V_w(R_o)$ for $\Delta \neq 1$, but $V_w(R_s)$, say, where $R_s \gtrless R_o$ for an accelerating/decelerating foil. Assuming the mean velocity in the mid-plane of the foil is $\overline{V}$ as given by (31), R_s can be calculated by equating mass flows in the inflow and in the foil mid-plane, and hence $V_w(R_s)$ obtained. A modified value of $\overline{V}$ is now obtained from (31) substituting $V_w(R_s)$ for $V_w(R_o)$. If necessary still more accurate values of $\overline{V}$ can be obtained by taking further steps in the iteration, though for the values of Δ concerned here only the first step changed $\overline{V}$ significantly.

(b) Secondly, since the inflow velocity depends on radius and therefore varies over the surface of the foil, V_o must be replaced by $V_w(r)$ for $r = c(x) \pm s(x)$ in the statement of the boundary condition (2). This has the effect of inducing an additional bound-vortex distribution on the foil and hence changing the circulation around each section. Since this effect depends basically on the section-thickness distribution and the local velocity gradient of the inflow, the effect appears to be essentially a two-dimensional one. A good approximation to the axisymmetric case (at least for $\lambda \ll \infty$) should be obtained from the solution of the two-dimensional problem of an aerofoil in a shear flow. This has been dealt with by Tsien,[12] Sowyrda[13] and Vidal *et al*,[21] who shew that the shear flow induces a component of lift positive in the direction of increasing inflow velocity with magnitude given approximately by (*see* Ref. 21)

$$C_L = 2\pi \left[\frac{\tau}{4} + \frac{h}{16l} \cdot k_L^2\right] \tag{32}$$

where τ is the thickness/chord ratio, h is the maximum camber height, l the chord length and $k_L = \frac{l}{V_w}\frac{dV_w}{dr}$. The velocity V_w and the velocity gradient $\frac{dV_w}{dr}$ must be evaluated as in (a) on the streamline which stagnates on the leading edge of the foil rather than at the mean foil radius R_o. This difference is especially important in the particular experiments considered here, where, as will be described later, the foils were situated on the edge of an axisymmetric wake so that the velocity gradient $\frac{dV_w}{dr}$ varied significantly in the region of the radius of the foil section (i.e. $r \sim R_o$). As a result k_L varies for different foils in the same inflow. For example, $k_L = 0$ for the accelerating foil B.3, but $k_L = 0{\cdot}5$ for the decelerating foil B.1.

Equation (32) gives a measure of the change in lift, and hence circulation round a section due to the shear nature of the inflow. The estimate of the corresponding change in the mean velocity $\overline{V}$ is shown in Table 6.

(c) Thirdly, in order to take account of the rotational nature of the whole inflow, and not merely that which meets the foil section as discussed in (b) above, the free vorticity can be concentrated into one or more cylindrical vortex sheets, and hence the infow velocity field approximated by a series of step functions. The presence of the annular foil changes the strength of these vortex sheets, and hence alters the axial velocity in the mid-chord plane of the foil. The corresponding two-dimensional problem has been treated by Glauert[14, 15], using the method of images. Unlike the effect discussed in (b) above, the two-dimensional theory cannot be considered to offer a good approximation in this case, and so a three-dimensional approach was necessary. For a first calculation the single cylindrical vortex sheet representation of the shear flow was chosen, with radius equal to the measured displacement radius of the undisturbed shear flow. The sheet was assumed to be of finite length $l' \gg 1$, and the vortex distribution represented by a Birnbaum series, in exactly the same manner as for the annular foil with a centre-body (*see* Section 8) except that the boundary condition which determines the coefficients of the terms of the series now requires the pressure to be continuous across the vortex sheet.

It was found as is shown in Table 6 that this effect is very small, reducing the acceleration (or deceleration) component of the velocity by only 2 per cent. It was thus considered unnecessary, in the present case, to consider a more complex representation of vortex sheets or to consider the further correction made by Glauert,[14, 15] arising from the free vorticity of the flow interacting with and thereby modifying the bound vortex-distribution.

TABLE 6

Annular Foils in Shear Flow;

Mean Velocity in Mid-Chord Plane, $\overline{V}/V_o$

(1) *Predicted Values*

	Foil B1		Foil B2		Foil B3	
Freestream velocity ft/sec	100	180	100	180	100	180
$\overline{V}/V_o$—First estimate	0·57	0·58	0·73	0·75	1·06	1·08
Increments to $\overline{V}/V_o$ (a) ..	+0·01	+0·02	0·00	0·00	0·00	0·00
due to 3 secondary (b) ..	−0·05	−0·05	−0·01	−0·01	0·00	0·00
effects (c) ..	+0·01	+0·01	0·00	0·00	0·00	0·00
$\overline{V}/V_o$—Final estimate ..	0·54	0·56	0·72	0·74	1·06	1·08

(2) *Experimental Values* (*see* Section 10)

$\overline{V}/V_o$—Experimental values ..	0·53	0·56	0·73	0·75	1·06	1·07

10. *Experimental Results for Axisymmetric Shear Flow*

The axisymmetric shear inflow used in the experiments was the 'early wake' produced by a streamlined body of revolution. This was preferred to a boundary-layer type flow since the additional effect of a rigid boundary is eliminated; this effect had been studied separately as described in Section 8.

The body had an overall length of 10 ft. $7\frac{1}{2}$ in., a hemi-spherical nose of diameter 21 in., a parallel-sided cylindrical portion of diameter 21 in. and length 66 in., blending in to a conical tail 51 in. long with semi-angle $11\frac{1}{2}$ deg. (*see* Figure 10). The size of the body, which was made of fibreglass with a rough surface, was chosen so that its wake had a diameter equal to that of the foils.

The body was mounted on wires in the wind tunnel as shown in Figure 11. Velocity traverses were taken across the wake of the body at the intended position of the mid-chord plane of the foils, measurements being made in three radial directions, vertically upwards and across the horizontal diameter, and the results averaged at each radius. The tunnel speed V_0 was measured in the same plane with a pitot-static tube placed midway between the axis and the tunnel wall to allow for the large blockage effect of the body. At 100 ft/sec the displacement radius of the wake was 0·17 R_o, the mean velocity over the disc of radius R_o was $\overline{V}_w = 0{\cdot}82\ V_o$ and the velocity at radius $r = R_o$, $V_w(R_o) = 0{\cdot}965\ V_o$. At 180 ft/sec the displacement radius was 0·16 R_o, the mean velocity $\overline{V}_w = 0{\cdot}84\ V_o$ and $V_w(R_o) = 0{\cdot}985\ V_o$.

The annular foils of Set B were mounted in turn on a strut on the axis of the body, with mid-plane 2 ft behind the tail, centred by means of a detachable sting extending from the tail of the body. At this position the flow in the absence of the foils was axial, i.e. neither converging nor diverging.

Interior velocity traverses in the mid-chord plane of the three foils are shown in Figures 25, 26 and 27. Also given are some predicted curves, corresponding to the first-order theory discussed above, where the incremental velocity field produced by the foil is assumed to be the same as when the foil is in a uniform inflow with velocity $V_w(R_o)$. The mean values of the measured axial-velocity distribution over the mid-chord plane of the foil are shown in Table 6.

The measured pressure distributions on the foils in the wake inflow are shown in Figures 28, 29 and 30 for comparison with the uniform inflow case.

It is concluded from the results shown in Table 6 that the approximate theory outlined above adequately predicts the behaviour of the foils when in an axisymmetric shear inflow, at least for the foil geometry and type of shear flow considered here.

11. *Conclusions*

The mathematical model employed here for annular aerofoils at zero incidence in iniform inflow was based on inviscid flow theory together with a 74 per cent viscous correction to the uniform circulation distribution. It is concluded from these experiments that this is certainly adequate to predict the velocity distribution in the mid-chord plane of the foil, for foils with chord/diameter ratios in the range 0·75 to 1·00 and diffusion ratios in the range 0·65 to 1·00. This design procedure was not adequate, however, for the single accelerating foil tested. In this case a correction factor of 0·74 gave the design diffusion ratio as 1·19, while a correction factor of 1·00 (i.e. no correction at all) would be needed to give 1·24 the experimental value.

The predicted pressure distributions agreed reasonably well with experiment except for the first 20 per cent of the pressure face on each of the three foils measured and except for the whole of the suction face of the accelerating foil.

The experiments with the foils at incidence in a uniform flow indicate that there is a significant variation of lift slope with diffusion ratio. The difference from the invariant value predicted by inviscid theory may be attributed to the large cambers of the foils tested. This also accounts for leading edge separation

occurring at relatively small angles of incidence. This separation has the effect of slightly increasing the lift and appreciably increasing the profile drag at the higher incidences.

The effect of a concentric centre-body on the performance of the foils was found to be very small for centre-bodies with diameters not greater than half the mean diameter of the foil. The slight increase in perturbation velocity across the mid-plane of the foils was adequately predicted by an approximate calculation, in which the centre-body was represented by a finite distribution of vortex rings.

Three of the foils were tested when surrounding an axisymmetric shear flow (wake). As a first estimate to calculating the velocity in the mid-chord plane the perturbation velocity field produced by the foil was considered to be the same as is produced by the foil when lying in a uniform inflow with velocity equal to the velocity of the shear flow at the mean radius of the foil. The agreement between the resulting first estimate and experiment was found to be very good for two out of the three foils. However excellent agreement was obtained when three secondary 'interaction effects' were considered.

Acknowledgments

The authors wish to thank M. Cottam for help with the mathematical work and B. J. L. Hall, L. Wilkins, D. A. Leaver and A. J. Brown for performing the experiments, and gratefully acknowledge the work of members of the Admiralty Research Laboratory Drawing Office and Workshop in the manufacture of the models.

LIST OF SYMBOLS

A	Aspect ratio of the annular foil = (diameter)/(chord length)[$= 1/\lambda$]
b	Constant occurring in definition of constant vortex distribution γ_0
$c(x)$	Radius of camber line of the annular foil section
C_p	Pressure coefficient
C_L	Lift coefficient
C_D	Drag coefficient
C_{D_0}	Profile drag coefficient
C_{D_i}	Induced drag coefficient
D	Drag
h	Maximum camber height of a two-dimensional foil section
k, k_1, k_2, k_3	Arguments of complete elliptic integrals
K_n	Coefficients in Glauert expansion
l	Chord length of foil in axial direction
L	Lift
p	Static pressure
p_0	Free-stream static pressure
$q(x)$	Strength of source-ring distribution
q	Strength of an isolated source ring
r	Radial co-ordinate (cylindrical polars)
r_c	Radius of parallel portion of the centre-body
$r_i(x)$	Radius of inner face of foil
$r_0(x)$	Radius of outer face of foil
R_0	Mean radius of the annular aerofoil
Re	Reynolds number ($= V_0 l/\nu$)
$s(x)$	Half-thickness distribution of foil section
V	Total axial component of velocity
V_0	Uniform inflow velocity
$\overline{V}$	Mean velocity across mid-chord plane of the foil
V_w	Axial velocity in shear inflow
$\overline{V}_w$	Mean value of V_w in mid-chord plane of foil over the circle $0 \leqslant r \leqslant R_0$
v_r	Radial component of perturbation velocity produced by foil
v_x	Axial component of perturbation velocity produced by foil
v^*_{qr}	Regular part of radial component of velocity due to source-ring distribution
v_{qx}	Axial component of velocity due to source ring-distribution
$v_{\gamma_0 r}$	Radial component of velocity due to vortex-ring distribution
$v^*_{\gamma_0 x}$	Regular part of axial component of velocity due to vortex-ring distribution
$\bar{v}_q$	Mean axial velocity due to source-ring distribution in mid-chord plane of foil
$\bar{v}_{\gamma_0}$	Mean axial velocity due to vortex-ring distribution in mid-chord plane or foil

x	Axial co-ordinate (cylindrical polars)
x', x''	Dummy axial co-ordinates (cylindrical polars)
α	Angle of incidence of annular foil to uniform inflow
$\gamma_0(x)$	Strength of vortex-ring distribution for foil in uniform inflow
$\gamma(\theta, x)$	Strength of vortex-ring distribution on mean cylinder for foil at incidence
$\gamma_1(\theta, x)$	Strength of vortex-ring distribution due to incidence
$\gamma_2(\theta, x)$	Strength of axial vortex distribution
Γ	Strength of an isolated vortex ring
Δ	Diffusion ratio of foil ($= \overline{V}/V_0$)
θ	Polar angle co-ordinate (cylindrical polars)
λ	Chord/diameter ratio of foil $= l/2R_0$
μ, μ_1, μ_2	Argument of Legendre functions
ν	Kinematic viscosity
ξ	Non-dimensional axial co-ordinate (cylindrical polars) $= x/R_0$
ρ	Fluid density
τ	Aerofoil section thickness/chord ratio
ϕ	Eccentric angle of thin-aerofoil theory (also used as a dummy variable in definitions of elliptic integrals and Legendre functions in Appendix I)
ψ	Axisymmetric stream function

REFERENCES

No.	Author(s)	Title, etc.
1	D. Küchemann and J. Weber	*Aerodynamics of propulsion.* McGraw-Hill Publishing Co. 1953.
2	W. B. Morgan	A theory of the ducted propeller with a finite number of blades. University of California—Contract No. N-onr-222(30). 1961.
3	B. Thwaites	*Incompressible aerodynamics.* Oxford University Press. 1960.
4	J. A. Bagley, N. B. Kirby and P. J. Marcer	A method of calculating the velocity distribution on annular aerofoils in incompressible flow. A.R.C. R. & M. 3146. June, 1958.
5	D. E. Ordway, M. M. Sluyter and B. O. U. Sonnerup	Three-dimensional theory of ducted propellers. Therm Advanced Research Report TAR-TR 602. August, 1960.
6	D. E. Ordway and M. D. Greenberg	General harmonic solutions for the ducted propeller. Therm Advanced Research Report TAR-TR 613. August, 1961.
7	M. M. Sluyter	A computational program and extended tabulation of Legendre functions of second kind and half order. Therm Advanced Research Report TAR-TR 601. 1960.
8	G. R. Hough	The aerodynamic loading on streamlined ducted bodies. Therm Advanced Research Report TAR-TR 625. 1962.
9	J. Weissinger	Zur Aerodynamik des Ringflügels. I Die Druckverteilung dünner, fast drehsymmetrischer Flügel in Unterschallströmung. D.V.L. Bericht Nr 2. 1955. Also published in Zeitschrift fur Flugwissenschaften, Vol. 4, pp. 141–150. 1956.
10	H. S. Fletcher	Experimental investigation of lift, drag and pitching moment of five annular airfoils. NACA TN 4117. October, 1957.
11	H. J. Allen and E. W. Parkins	Characteristics of flow over inclined bodies of revolution. NACA RM A50LO7. March, 1951.
12	H. S. Tsien	Symmetric Joukowsky airfoils in shear flow. *Quarterly of Applied Maths.* Vol. I, pp. 130–148, 1943.
13	A. Sowyrda	Theory of cambered Joukowsky airfoils in shear flow. Cornell Aeronautical Laboratory Rep. Nr AI-1190-A-2. 1958.
14	H. Glauert	Influence of a uniform jet on the lift of an aerofoil. A.R.C. R. & M. 1602. 1934.
15	H. Glauert	Lift and drag of a wing spanning a free jet. A.R.C. R. & M. 1603. (1934).
16	L. Meyerhoff and A. B. Finkelstein	On the theories of duct shape for a ducted propeller. Polytechnic Institute of Brooklyn, PIBAL Rep. No. 484. 1955.
17	E. Jahnke and F. Emde	*Tables of functions.* Teubner Leipzig and Berlin. 1933.

REFERENCES—*continued*

No.	*Author(s)*	*Title, etc.*
18	National Bureau of Standards	*Tables of Associated Legendre functions.* Columbia Univ. Press. 1945.
19	D. Küchemann	Tafeln für die Stromfunktion und die Geschwinddigkeitskomponenten von Quellring and Wirbelring. Jahrbuch 1940 der Deutschen Luftfahtforschung, pp. I547–I564.
20	G. N. Watson	*Treatise on the theory of Bessel functions.* Cambridge University Press. 2nd edition. 1952.
21	R. J. Vidal, J. T. Curtis and J. H. Hillier	The influence of two-dimensional stream shear on airfoil maximum lift. Cornell Aero. wab. Rep. No. A1–1190–A–7. 1961.

APPENDIX I

Mathematical Expressions for Induced Velocities

The basic expressions needed in the design of the annular foils are those for the velocity fields of a source ring and of a vortex ring. These are variously expressed in terms of Bessel functions, complete elliptic integrals and Legendre functions of the second kind and half order.

Bessel functions are the most convenient for constructing solutions to potential flow problems, as the powerful methods of orthogonal functions and integral transforms can be employed, but they are of little use when it comes to computing the numerical values of the expressions. For the application of Bessel functions to the theory of annular aerofoils see Meyerhoff and Finkelstein[16].

The expressions in terms of complete elliptic integrals are those most widely used for numerical computation in annular aerofoil theory (*see* Refs. 1, 2 and 16), since they are extensively tabulated, e.g. Jahnke and Emde[17]. The only drawback to the use of elliptic integrals, at least in desk machine calculations, is that the expressions tend to be rather long and unsymmetrical.

The recent series of reports published by Therm[5,6,7,8] on the theory of annular aerofoils uses Legendre functions of the second kind and half order. The expressions for the velocity components of source and vortex rings in terms of Legendre functions, as can be seen from the expressions below, are simpler than the corresponding expressions using elliptic integrals. An extended tabulation of these Legendre functions has been carried out by Therm,[7] which supplements the National Bureau of Standards Tables,[18] to facilitate the use of these expressions with a desk machine. The Legendre function expressions are thus recommended as being those best suited to computations on a desk machine.

Tables of the induced velocities of a source and vortex ring, and of certain distributions of vortex rings are given in the Appendix of Reference 1, and also in an extended tabulation by Küchemann[19]. However it was found for the computations in the design of the foils presented in this report that these tables were not sufficiently accurate, and the induced velocities had to be evaluated from the analytic expressions.

These various expressions for the induced velocities are given below, together with definitions of the various functions involved.

Definitions

(*a*) Bessel functions can be defined in various ways, *see* for example Watson. [20] The most useful definition for application to potential flow theory, however, is to regard the Bessel function of the first kind and order n, i.e. $J_n(x)$, as the non-singular solution of Bessel's Equation :

$$\frac{d^2y}{dx^2}+\frac{1}{x}\frac{dy}{dx}+\left(1-\frac{n^2}{x^2}\right)y = 0. \qquad \text{A.1.}$$

(b) Complete elliptic integrals of the first, second and third kind are defined by

$$K(k) = \int_0^{\pi/2} \frac{1}{\sqrt{1-k^2\sin^2\phi}}\,d\phi\,, \qquad \text{A.2.}$$

$$E(k) = \int_0^{\pi/2} \sqrt{1-k^2\sin^2\phi}\,d\phi\,, \qquad \text{A.3.}$$

$$D(k) = \int_0^{\pi/2} \frac{\sin^2\phi}{\sqrt{1-k^2\sin^2\phi}}\,d\phi = \frac{K(k)-E(k)}{k^2}. \qquad \text{A.4.}$$

(c) The Legendre function of second kind and half order $Q_{n-\frac{1}{2}}(\mu)$ can be defined by

$$Q_{n-\frac{1}{2}}(\mu) = \int_{-\pi/2}^{+\pi/2} \frac{\cos 2n\phi}{[2(\mu-1)+4\sin^2\phi]^{\frac{1}{2}}}\, d\phi\,. \qquad \text{A.5.}$$

The expressions below give the velocity components at the general point (ρ,ξ) due to a source (or vortex) ring, centre at the origin and of radius R_0 in the plane $\xi = 0$. The non-dimensional co-ordinates (ρ,ξ) are given by $\rho = r/R_0$, $\xi = x/R_0$.

Source Ring—Radial Velocity Component.

$$v_{S.R,r} = \frac{q}{2R_0}\int_0^\infty s\, J_0(s)J_1(s\rho)e^{-s|\xi|}\, ds \qquad \text{A.6.}$$

$$= \frac{q}{2\pi R_0}\ \frac{1}{\rho\sqrt{\xi^2+(\rho+1)^2}}\left[K(k) - \left[1-\frac{2\rho(\rho-1)}{\xi^2+(\rho-1)^2}\right]\mathrm{E}(k)\right] \qquad \text{A.7.}$$

$$= \frac{q}{2\pi R_0}\left[\frac{Q'_{\frac{1}{2}}(\mu)}{\rho^{3/2}} - \frac{Q'_{-\frac{1}{2}}(\mu)}{\rho^{1/2}}\right]. \qquad \text{A.8.}$$

Source Ring—Axial Velocity Component

$$v_{S.R,x} = \pm\frac{q}{2R_0}\int_0^\infty s\, J_0(s)J_0(s\rho)\, e^{-s|\xi|}ds \text{ as } \xi \gtrless 0 \qquad \text{A.9.}$$

$$= \pm\frac{q}{2\pi R_0}\ \frac{2\xi E(k)}{(\xi^2+(\rho+1)^2)^{\frac{1}{2}}(\xi^2+(\rho-1)^2)} \text{ as } \xi \gtrless 0 \qquad \text{A.10.}$$

$$= \mp\ \frac{q}{2\pi R_0}\ \frac{\xi . Q'_{-\frac{1}{2}}(\mu)}{\rho^{3/2}}. \qquad \text{as } \xi \gtrless 0 \qquad \text{A.11.}$$

Vortex Ring—Radial Velocity Component.

$$v_{V.R,r} = \pm\frac{\Gamma}{2R_0}\int_0^\infty s\, J_1(s)J_1(s\rho)\mathrm{e}^{-s|\xi|}ds \text{ as } \xi \gtrless 0 \qquad \text{A.12.}$$

$$= \mp\ \frac{\Gamma}{2\pi R_0}\ \frac{\xi}{\rho\sqrt{\xi^2+(\rho+1)^2}}\left(K(k) - \left[1+\frac{2\rho}{\xi^2+(\rho-1)^2}\right]E(k)\right)$$

$$\text{as } \xi \gtrless 0 \qquad \text{A.13.}$$

$$= \mp\ \frac{\Gamma}{2\pi R_0}\ \frac{\xi Q'_{\frac{1}{2}}(\mu)}{\rho^{3/2}} \qquad \text{as } \xi \gtrless 0. \qquad \text{A.14.}$$

Vortex Ring—Axial Velocity Component.

$$v_{V.R,x} = \frac{\Gamma}{2R_0}\int_0^\infty \mathrm{s}\, J_1(s)J_0(s\rho)\, e^{-s|\xi|}ds \qquad \text{A.15.}$$

$$= \frac{\Gamma}{2\pi R_0}\ \frac{1}{\sqrt{\xi^2+(\rho+1)^2}}\left(K(k) - \left[1+\frac{2(\rho-1)}{\xi^2+(\rho-1)^2}\right]\ E(k)\right) \qquad \text{A.16.}$$

$$= \frac{\Gamma}{2\pi R_0}\left[\frac{Q'_{\frac{1}{2}}(\mu)}{\rho^{1/2}} - \frac{Q'_{-\frac{1}{2}}(\mu)}{\rho^{3/2}}\right] \qquad \text{A.17.}$$

The argument of the elliptic integrals, k, is given by

$$k = +\sqrt{\frac{4\rho}{(\rho+1)^2+\xi^2}} \qquad \text{A.18.}$$

and that of the Legendre function, μ, by

$$\mu = \frac{\rho^2+1+\xi^2}{2\rho}. \qquad \text{A.19.}$$

In computing the camber gradient $c'(x)$, these velocities are evaluated on the mean cylinder $r = R_0$, $o \leqslant x \leqslant l$, and thus the non-dimensional ρ in the above equations takes the value unity, and the expressions are correspondingly simpler.

Induced Velocities due to Constant Vortex Distribution on Cylinder.

For the particularly simple case where the vortex strength is constant along the foil's mean cylinder $r = R_0$, $o \leqslant x \leqslant l$, analytic expressions for the induced velocities evaluated on the mean cylinder can be obtained. Such expressions in terms of elliptic integrals are given in the Appendix of Reference 1, and the velocity components are also tabulated for various value of λ, the chord/diameter ratio. If the strength density of the vortex ring distribution is $\gamma_0(x) = 2\pi V_0 b$, then in terms of complete elliptic integrals,

$$v_{\gamma_0 r}(x, R_0) = -V_0 b[k\,(K(k)-2D(k))]_{k_y}^{k2} \qquad \text{A.20.}$$

and

$$v^*_{\gamma_0 x}(x, R_0) = V_0 b\left[\sqrt{1-k_1^2}\,K(k_1)+\sqrt{1-k_2^2}\,K(k_2)\right] \qquad \text{A.21}$$

where

$$k_1 = +\sqrt{\frac{4}{4+\xi^2}},\ k_2 = +\sqrt{\frac{4}{4+(2\lambda-\xi)^2}}. \qquad \text{A.22.}$$

A particularly simple expression can be obtained for the radial component of the velocity in terms of Legendre functions:

$$v_{\gamma_0 r}(x, R_0) = V_0 b[Q_{\frac{1}{2}}(\mu)]_{\mu 1}^{\mu 2} \qquad \text{A.23.}$$

where

$$\mu_1 = 1+\tfrac{1}{2}\xi^2 \text{ and } \mu_2 = 1+\tfrac{1}{2}(2\lambda-\xi)^2. \qquad \text{A.24.}$$

The significance of the asterisk in A.21 is, as is used in the text, to emphasise that $v^*_{\gamma_0 x}$ is only the regular part of the axial velocity obtained by taking the Cauchy principal value of the integral.

It is necessary in the design procedure to evaluate the mass flow through the foil, produced by the vortex distribution. An analytic expression can be obtained for the mean velocity v_{γ_0} over the circle $x = 0$, $r \leqslant R_0$. In terms of the Stokes stream function the mean velocity for a vortex ring is given by

$$\pi R_0^2 \bar{v}_{\gamma_0} = 2\pi[\psi(0, R_0)-\psi(0, 0)].$$

The stream function of a vortex ring is given by

$$\psi_{V.R.} = \frac{\Gamma R_0}{2\pi}\,\rho^{\frac{1}{2}}k[K(k)-2D(k)]. \qquad \text{A.25.}$$

Hence putting $\rho = 1 (r = R_0)$ and integrating over the length of the mean cylinder, the following expression is obtained for

$$\bar{v}_{\gamma_0} = 8\sqrt{1-k_3^2}D(k_3)V_0 b \qquad \text{A.26.}$$

where

$$k_3 = +\sqrt{\frac{4}{\lambda^2+4}}. \qquad \text{A.27.}$$

General Source Ring and Vortex Ring Distributions.

The induced velocities due to the source ring distribution whose strength is given by (6), and of a general vortex ring distribution cannot be evaluated analytically and the integrations must be carried out by numerical methods, using the expressions for the velocity field of source and vortex rings given in this Appendix.

In particular the expressions for the radial components induced on the mean cylinder by the source and vortex ring distributions, needed to solve equation (5), can be obtained from equations A.7 and A.13, putting $\rho = 1$ $(r = R_0)$ and substituting for k from A18, and integrating over the length of the foil.

They are

$$v^*_{q_r}(x, R_0) \equiv v^*_{q_r}(\xi, 1) = \frac{1}{2\pi}\int_0^{2\lambda} q(\xi')[\tfrac{1}{2}k^3 D(k)]\,d\xi' \qquad \text{A.28.}$$

and

$$v_{\gamma_{0r}}(x, R_0) \equiv v_{\gamma_{0r}}(\xi, 1) = \frac{1}{2\pi}\int_0^{2\lambda} \gamma_0(\xi')\,k^2 \left[k' D(k) - \frac{E(k)}{2k'}\right] d\xi' \qquad \text{A.29.}$$

where

$$k^2 = 4\Big/((\xi-\xi')^2+4) \text{ and } k'^2 = 1-k^2. \qquad \text{A.30.}$$

APPENDIX II

Design Ordinates of the Six Annular Aerofoils

The ordinates of the two sets of annular foils are tabulated below. These ordinates were given at twenty equally-spaced chordwise positions, plus two extra points near the leading edge where the thickness distribution varies rapidly. $r_i(x)$ denotes the inner face of the foil and $r_0(x)$ the outer face. The ordinates are given in inches.

Foils of Set A, $\lambda = 1{\cdot}0$

		A.1. $\Delta = 6{\cdot}63$		A.2. $\Delta = 0{\cdot}82$		A.3. $\Delta = 1{\cdot}00$	
x/l	x ins	$r_i(x)$	$r_0(x)$	$r_i(x)$	$r_0(x)$	$r_i(x)$	$r_0(x)$
0·00	0	5·55	5·55	5·69	5·69	5·93	5·93
0·005	0·06	5.53	5.68	5·66	5·79	5·88	5·99
0·025	0·30	5·55	5·86	5·62	5·93	5·79	6·10
0·05	0·60	5·59	6·00	5·62	6·04	5·75	6·18
0·10	1·20	5·67	6·22	5·64	6·19	5·71	6·27
0·15	1·80	5·74	6·37	5·66	6·30	5·68	6·33
0·20	2·40	5·80	6·48	5·69	6·37	5·68	6·37
0·25	3·00	5·85	6·56	5·71	6·42	5·68	6·39
0·30	3·60	5·89	6·61	5·72	6·45	5·68	6·40
0·35	4·20	5·93	6·64	5·75	6·47	5·69	6·40
0·40	4·80	5·95	6·65	5·77	6·47	5·70	6·39
0·45	5·40	5·98	6·65	5·79	6·46	5·71	6·38
0·50	6·00	5·99	6·63	5·80	6·44	5·72	6·36
0·55	6·60	6·00	6·60	5·82	6·40	5·73	6·33
0·60	7·20	6·01	6·55	5·83	6·37	5·75	6·30
0·65	7·80	6·00	6·50	5·83	6·33	5·76	6·26
0·70	8·40	5·99	6·43	5·83	6·27	5·78	6·22
0·75	9·00	5·97	6·34	5·83	6·21	5·79	6·17
0·80	9·60	5·93	6·25	5·82	6·13	5·81	6·13
0·85	10·20	5·88	6·13	5·80	6·05	5·82	6·08
0·90	10·80	5·80	5·98	5·77	5·95	5·82	6·02
0·95	11·40	5·66	5·82	5·69	5·85	5·82	5·98
1·00	12·00	5·47	5·52	5·60	5·66	5·84	5·90

Foils of Set B $\lambda = 0{\cdot}75$

		B.1. $\Delta = 0{\cdot}73$		B.2. $\Delta = 0{\cdot}91$		B.3. $\Delta = 1{\cdot}19$	
x/l	x ins	$r_i(x)$	$r_0(x)$	$r_i(x)$	$r_0(x)$	$r_i(x)$	$r_0(x)$
0·00	0·00	5·58	5·58	5·84	5·84	6·16	6·16
0·005	0·045	5·57	5·66	5·81	5·90	6·10	6·19
0·025	0·225	5·57	5·80	5·76	6·00	6·00	6·24
0·05	0·45	5·60	5·92	5·75	6·07	5·93	6·25
0·10	0·90	5·66	6·08	5·74	6·16	5·48	6·26
0·15	1·35	5·71	6·19	5·75	6·23	5·78	6·26
0·20	1·80	5·76	6·27	5·75	6·27	5·74	6·26
0·25	2·25	5·80	6·33	5·76	6·30	5·72	6·25
0·30	2·70	5·83	6·37	5·77	6·31	5·70	6·24
0·35	3·15	5·86	6.40	5·79	6·32	5·70	6·23
0·40	3·60	5·89	6·41	5·80	6·32	5·70	6·22
0·45	4·05	5·91	6·41	5·81	6·32	5·70	6·20
0·50	4·50	5·92	6·40	5·82	6·30	5·71	6·19
0·55	4·95	5·93	6·38	5·84	6·28	5·72	6·17
0·60	5·40	5·93	6·35	5·85	6·26	5·74	6·16
0·65	5·85	5·93	6·30	5·86	6·23	5·77	6·14
0·70	6·30	5·92	6·25	5·87	6·20	5·80	6·13
0·75	6·75	5·90	6·19	5·87	6·16	5·83	6·12
0·80	7·20	5·90	6·11	5·87	6·11	5·87	6·11
0·85	7·65	5·84	6·03	5·87	6·06	5·91	6·10
0·90	8·10	5·78	5·92	5·87	6·00	5·97	6·10
0·95	8·55	5·69	5·79	5·84	5·94	6·03	6·12
1·00	9·00	5·54	5·58	5·80	6·12	6·12	6·16

APPENDIX III

Tabulated Pressure Distributions on Annular Aerofoils at Incidence

The pressure distributions for the foils at incidence are presented here in the form of a pressure coefficient defined by equation (11) for all three foils of Set B. All results presented here were made with the tunnel speed of 100 ft/sec and when the boundary layers on the foils were not being tripped. The measurements were made at incidences of −10 deg (2·5 deg) +10 deg on both the inner and outer faces of the foils (*see* Fig. 2 for notation and definition of positive and negative incidence).

*Foil B.*1., *Inner Face* C_p

x/l / $\alpha°$	0·05	0·10	0·20	0·30	0·40	0·50*	0·70	0·85	x/l / $\alpha°$
−10·0	−0·02	−0·05	−0·08	−0·09	−0·04		+0·19	+0·26	−10·0
− 7·5	−0·07	−0·08	−0·04	+0·09	+0·23		+0·40	+0·40	− 7·5
− 5·0	−0·20	−0·03	+0·27	+0·38	+0·41		+0·46	+0·45	− 5·0
− 2·5	+0·19	+0·27	+0·37	+0·42	+0·45		+0·50	+0·50	− 2·5
0·0	+0·30	+0·36	+0·43	+0·47	+0·48		+0·51	+0·51	0·0
+ 2·5	+0·43	+0·44	+0·47	+0·50	+0·51		+0·53	+0·51	+ 2·5
+ 5·0	+0·51	+0·48	+0·50	+0·50	+0·50		+0·52	+0·48	+ 5·0
+ 7·5	+0·59	+0·53	+0·52	+0·52	+0·51		+0·51	+0·49	+ 7·5
+10·0	+0·66	+0·58	+0·55	+0·52	+0·49		+0·49	+0·46	+10·0

*Foil B.*1., *Outer Face,* C_p

x/l / $\alpha°$	0·05	0·10	0·20	0·30	0·40	0·50*	0·70	0·85	x/l / $\alpha°$
−10·0	+0·33	+0·07	−0·12	−0·20	−0·24		−0·21	−0·17	−10·0
− 7·5	+0·21	−0·05	−0·21	−0·27	−0·29		−0·26	−0·19	− 7·5
− 5·0	+0·11	−0·16	−0·28	−0·33	−0·34		−0·28	−0·22	− 5·0
− 2·5	−0·04	−0·27	−0·37	−0·39	−0·38		−0·30	−0·24	− 2·5
0·0	−0·23	−0·41	−0·45	−0·44	−0·41		−0·30	−0·22	0·0
+ 2·5	−0·43	−0·55	−0·53	−0·49	−0·44		−0·30	−0·20	+ 2·5
+ 5·0	−0·60	−0·65	−0·58	−0·53	−0·48		−0·27	−0·17	+ 5·0
+ 7·5	−0·79	−0·75	−0·65	−0·56	−0·46		−0·23	−0·14	+ 7·5
+10·0	−0·98	−0·90	−0·70	−0·59	−0·49		−0·23	−0·14	+10·0

*A blockage formed in the length of hyperdermic tubing inside the foil, leading away from this pressure point during the manufacture of the foil, and hence no pressure measurements could be made at this station.

Foil B.2., Inner Face, C_p

x/l / $\alpha°$	0·05	0·10	0·20	0·30	0·40	0·50	0·70	0·85	x/l / $\alpha°$
−10·0	−0·97	−0·56	−0·53	−0·19	−0·02	+0·02	+0·09	+0·11	−10·0
− 7·5	−0·57	−0·36	−0·17	−0·06	−0·02	+0·04	+0·11	+0·14	− 7·5
− 5·0	−0·43	−0·24	−0·10	0·00	+0·06	+0·06	+0·13	+0·15	− 5·0
− 2·5	−0·23	−0·12	−0·03	+0·07	+0·08	+0·10	+0·15	+0·16	− 2·5
0·0	−0·04	+0·02	+0·06	+0·10	+0·12	+0·13	+0·17	+0·19	0·0
+ 2·5	+0·12	+0·12	+0·12	+0·15	+0·15	+0·13	+0·18	+0·19	+ 2·5
+ 5·0	+0·25	+0·22	+0·19	+0·19	+0·17	+0·15	+0·19	+0·20	+ 5·0
+ 7·5	+0·34	+0·27	+0·23	+0·22	+0·19	+0·17	+0·18	+0·19	+ 7·5
+10·0	+0·45	+0·33	+0·27	+0·24	+0·20	+0·18	+0·18	+0·19	+10·0

Foil B.2., Outer Face, C_p

x/l / $\alpha°$	0·05	0·10	0·20	0·30	0·40	0·50	0·50	0·85	x/l / $\alpha°$
−10·0	+0·36	+0·17	+0·02	−0·02	−0·06	−0·06	−0·06	−0·03	−10·0
− 7·5	+0·31	+0·10	−0·03	−0·07	−0·09	−0·07	−0·08	−0·03	− 7·5
− 5·0	+0·15	−0·01	−0·10	−0·13	−0·14	−0·13	−0·10	−0·06	− 5·0
− 2·5	−0·01	−0·14	−0·20	−0·17	−0·17	−0·15	−0·12	−0·06	− 2·5
0·0	−0·18	−0·26	−0·28	−0·23	−0·21	−0·18	−0·14	−0·08	0·0
+ 2·5	−0·37	−0·38	−0·34	−0·28	−0·24	−0·21	−0·14	−0·06	+ 2·5
+ 5·0	−0·54	−0·50	−0·39	−0·33	−0·26	−0·22	−0·12	−0·06	+ 5·0
+ 7·5	−0·74	−0·62	−0·45	−0·35	−0·29	−0·23	−0·12	−0·05	+ 7·5
+10·0	−0·81	−0·68	−0·48	−0·36	−0·29	−0·23	−0·11	−0·03	+10·0

Foil B.3., Inner Face, C_p

x/l / $\alpha°$	0·05	0·10	0·20	0·30	0·40	0·50	0·70	0·85	x/l / $\alpha°$
−10·0	−1·61	−1·36	−1·10	−0·90	−0·76	−0·68	−0·48	−0·32	−10·0
− 7·5	−1·34	−1·18	−1·04	−0·87	−0·73	−0·66	−0·50	−0·35	− 7·5
− 5·0	−0·99	−0·92	−0·88	−0·74	−0·68	−0·58	−0·44	−0·31	− 5·0
− 2·5	−0·78	−0·81	−0·81	−0·73	−0·68	−0·61	−0·48	−0·35	− 2·5
0·0	−0·53	−0·64	−0·71	−0·67	−0·63	−0·61	−0·53	−0·35	0·0
+ 2·5	−0·31	−0·48	−0·60	−0·59	−0·57	−0·55	−0·48	−0·36	+ 2·5
+ 5·0	−0·14	−0·34	−0·50	−0·52	−0·53	−0·53	−0·46	−0·36	+ 5·0
+ 7·5	+0·01	−0·22	−0·42	−0·47	−0·49	−0·50	−0·44	−0·37	+ 7·5
+10·0	+0·12	−0·13	−0·36	−0·42	−0·46	−0·47	−0·42	−0·36	+10·0

Foil B.3., Outer Face, C_p

x/l / $\alpha°$	0·05	0·10	0·20	0·30	0·40	0·50	0·70	0·85	x/l / $\alpha°$
−10·0	+0·41	+0·30	+0·17	+0·15	+0·13	+0·13	+0·13	+0·14	−10·0
− 7·5	+0·31	+0·21	+0·13	+0·10	+0·10	+0·10	+0·11	+0·14	− 7·5
− 5·0	+0·17	+0·12	+0·06	+0·06	+0·06	+0·07	+0·11	+0·13	− 5·0
− 2·5	+0·06	+0·03	+0·01	+0·03	+0·04	+0·06	+0·08	+0·10	− 2·5
0·0	−0·12	−0·08	−0·07	−0·04	−0·01	+0·01	+0·07	+0·09	0·0
+ 2·5	−0·26	−0·18	−0·10	−0·04	−0·03	0·00	+0·07	+0·07	+ 2·5
+ 5·0	−0·36	−0·27	−0·16	−0·07	−0·05	−0·01	+0·04	+0·07	+ 5·0
+ 7·5	−0·87	−0·36	−0·15	−0·07	−0·04	−0·03	+0·04	+0·07	+ 7·5
+10·0	−0·73	−0·72	−0·52	−0·21	−0·07	−0·01	+0·04	+0·06	+10·0

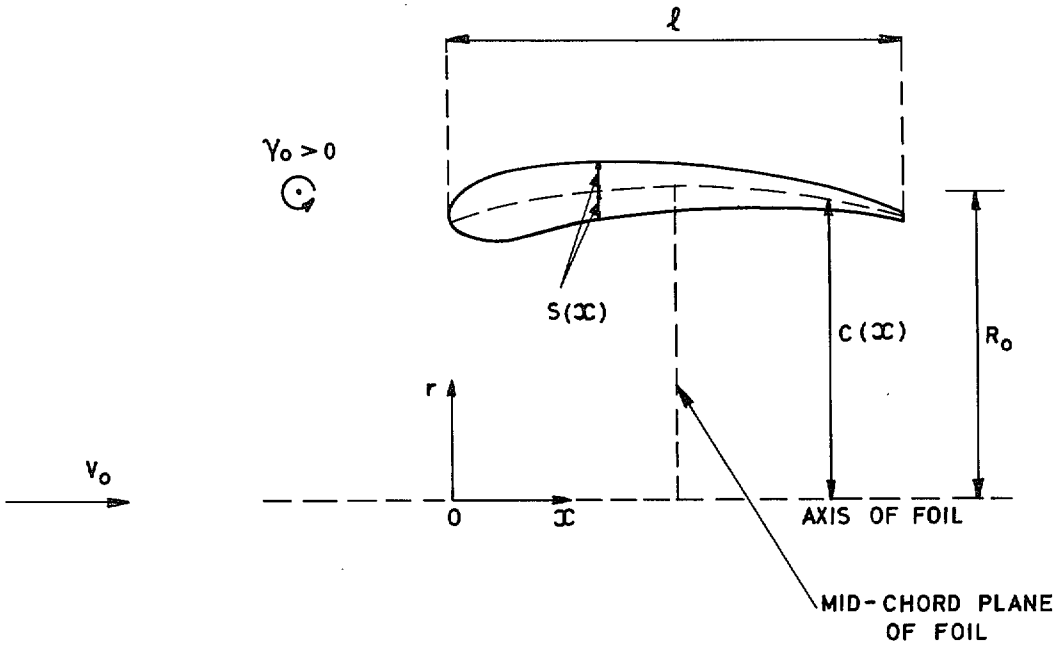

FIG. 1. Annular aerofoil section in design condition.–notation.

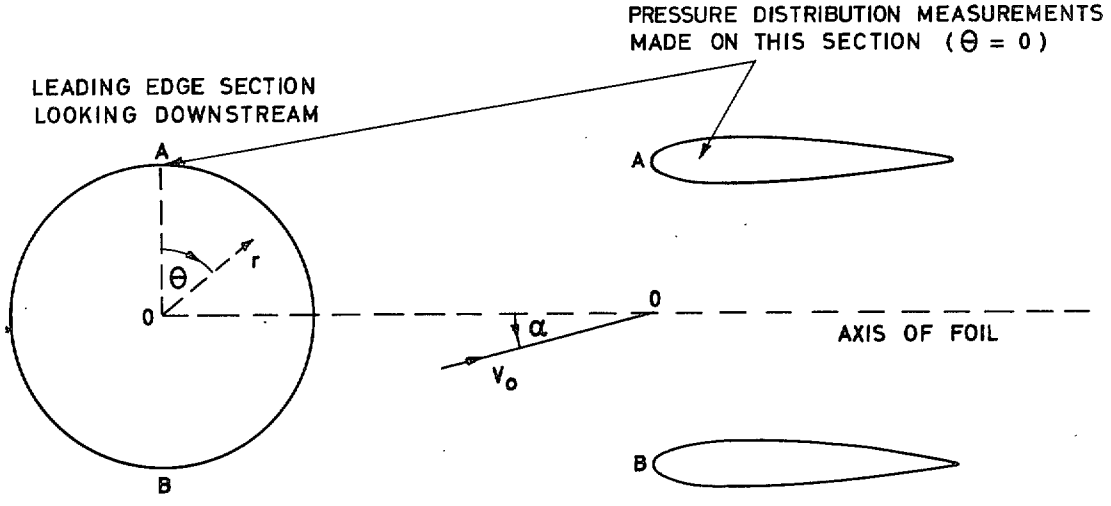

FIG. 2. Annular aerofoil at incidence.–notation.

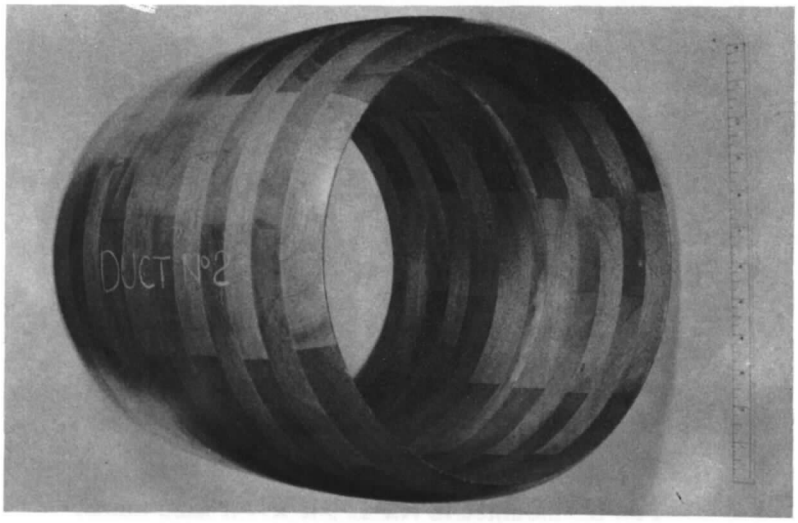

FIG. 3. Foil A2 (chord diameter ratio = 1, design diffusion ratio = 0·82).

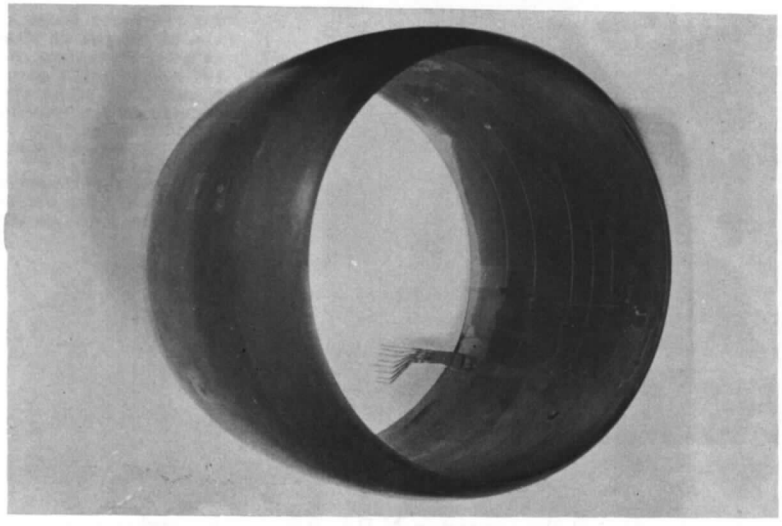

FIG. 4. Foil B1 (chord diameter ratio = 0·75, design diffusion ratio = 0·73).

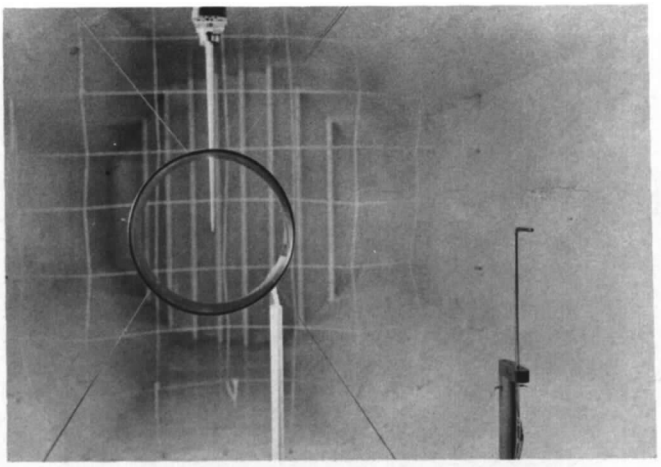

FIG. 5. Foil B.3 mounted in N.P.L. 9 ft × 7 ft wind tunnel.

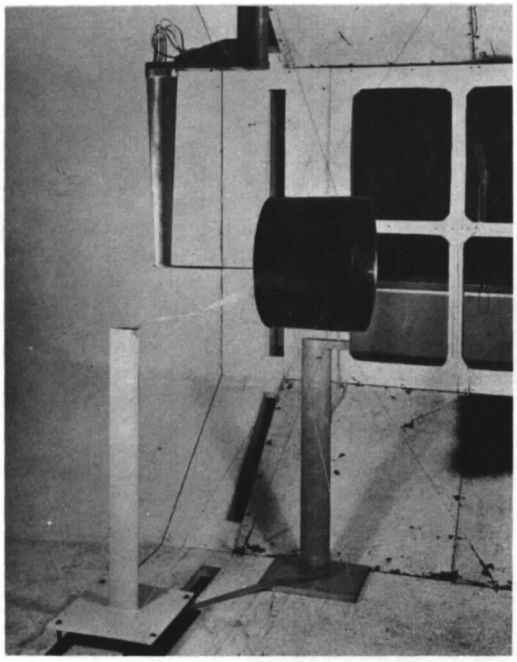

THE FIVE-HOLE PROBE ON THE AXIS OF THE FOIL, IS MOUNTED ON AN A.R.L. TRAVERSING GEAR. THE TUNNEL SPEED IS MEASURED BY THE PITOT STATIC TUBE MOUNTED ON A STREAMLINE STRUT ATTACHED TO THE TUNNEL FLOOR. (SEEN CLEARLY IN FIGURE 5) THE TRAILING FLEXIBLE TUBES, FOR SURFACE PRESSURE MEASUREMENTS, ARE LEAD OUT OF THE TUNNEL VIA A STREAMLINE STRUT.

FIG. 6. Foil B.3 mounted in N.P.L. 9 ft × 7 ft wind tunnel.

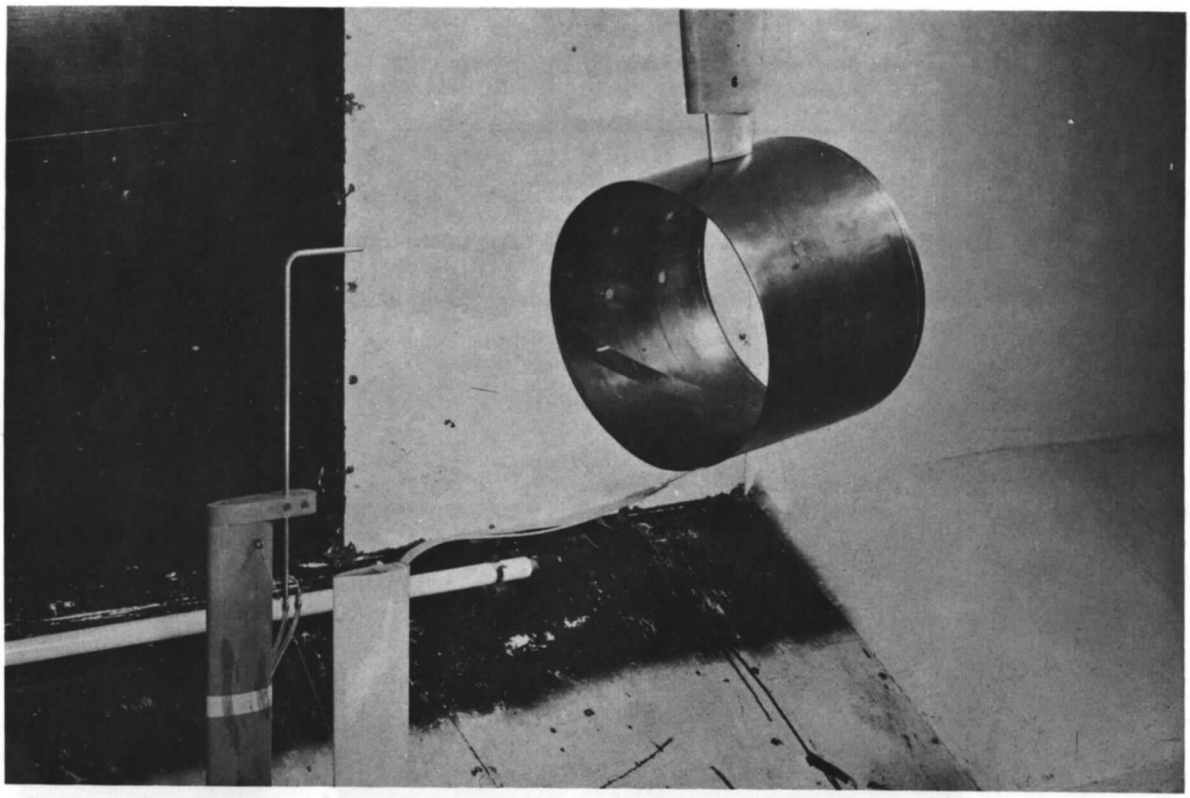

FIG. 7. Foil B.3. Mounted on strut for incidence measurements.

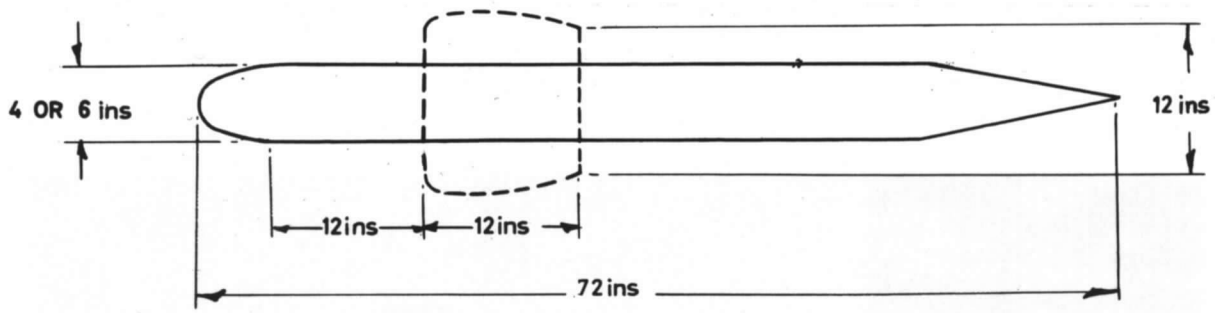

FIG. 8. Annular foil with centre-body experimental arrangement.

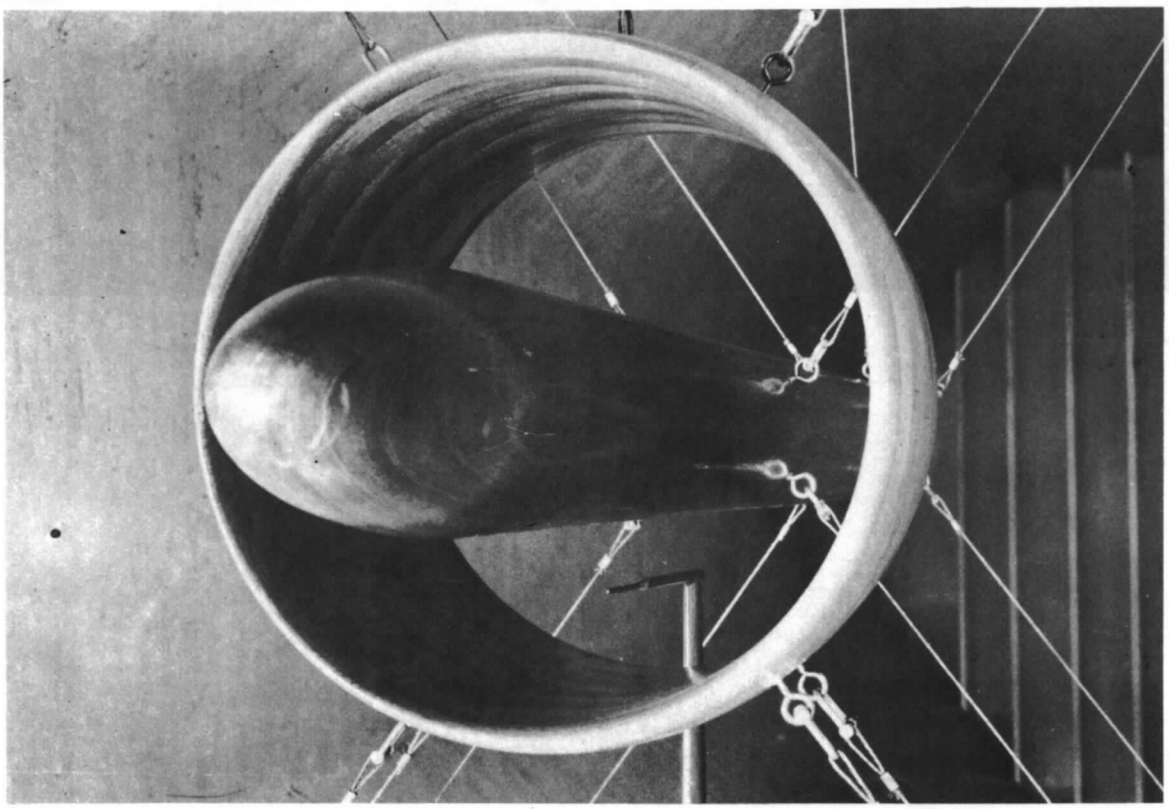

FIG. 9. Foil A3 mounted with 4 ins. diameter centre-body.

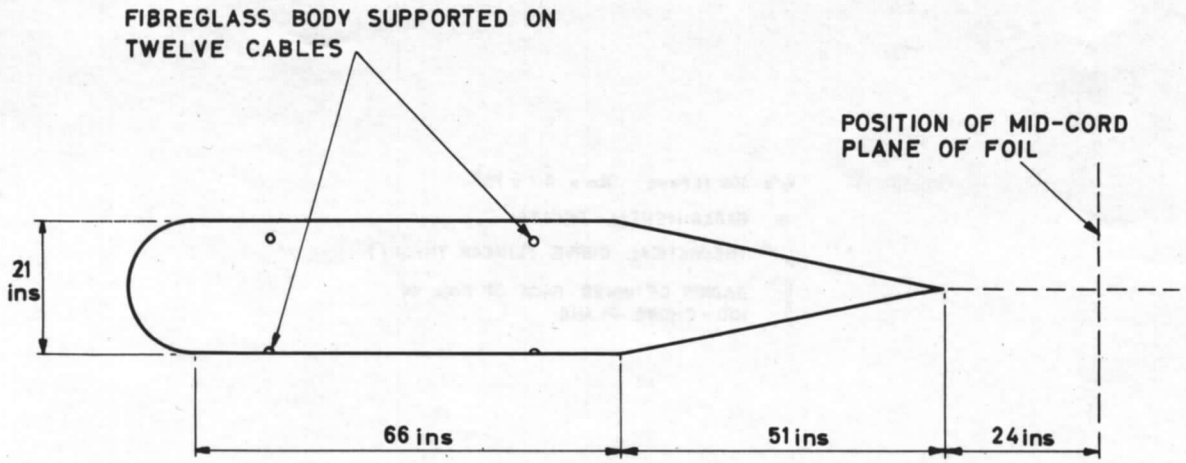

FIG. 10. Annular foil in axisymmetric shear flow experimental rig.

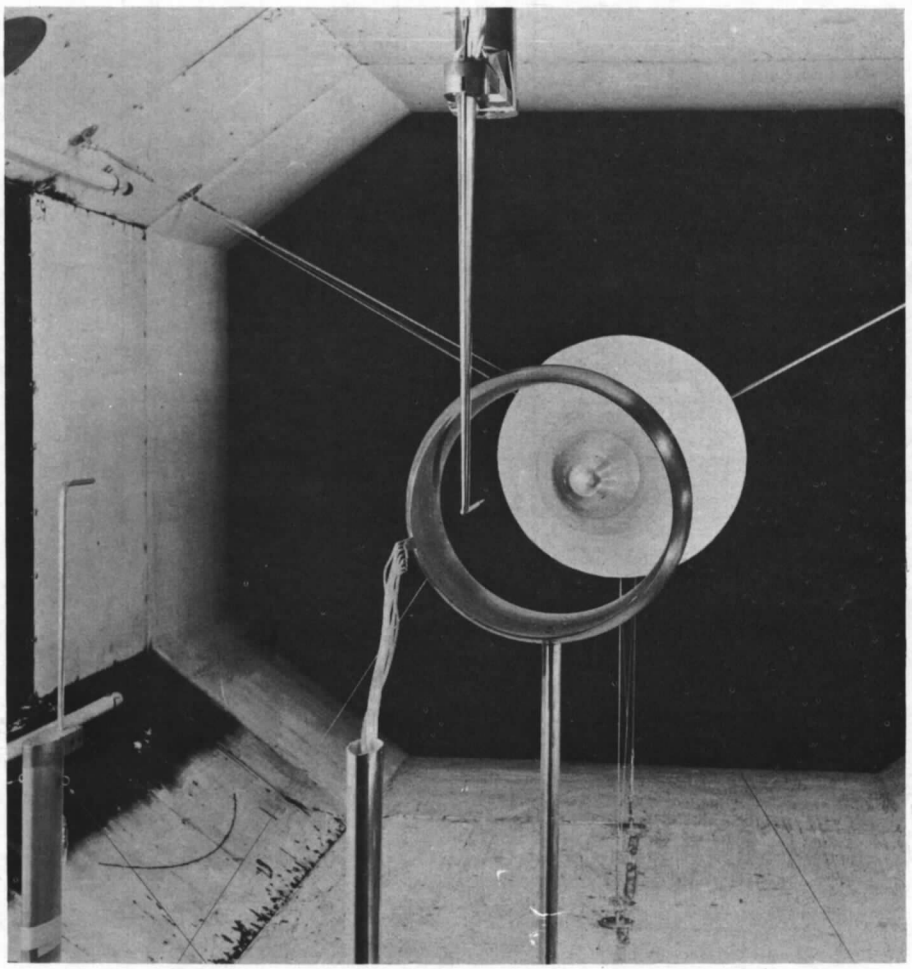

FIG. 11. Foil B2 mounted behind fibreglass body.

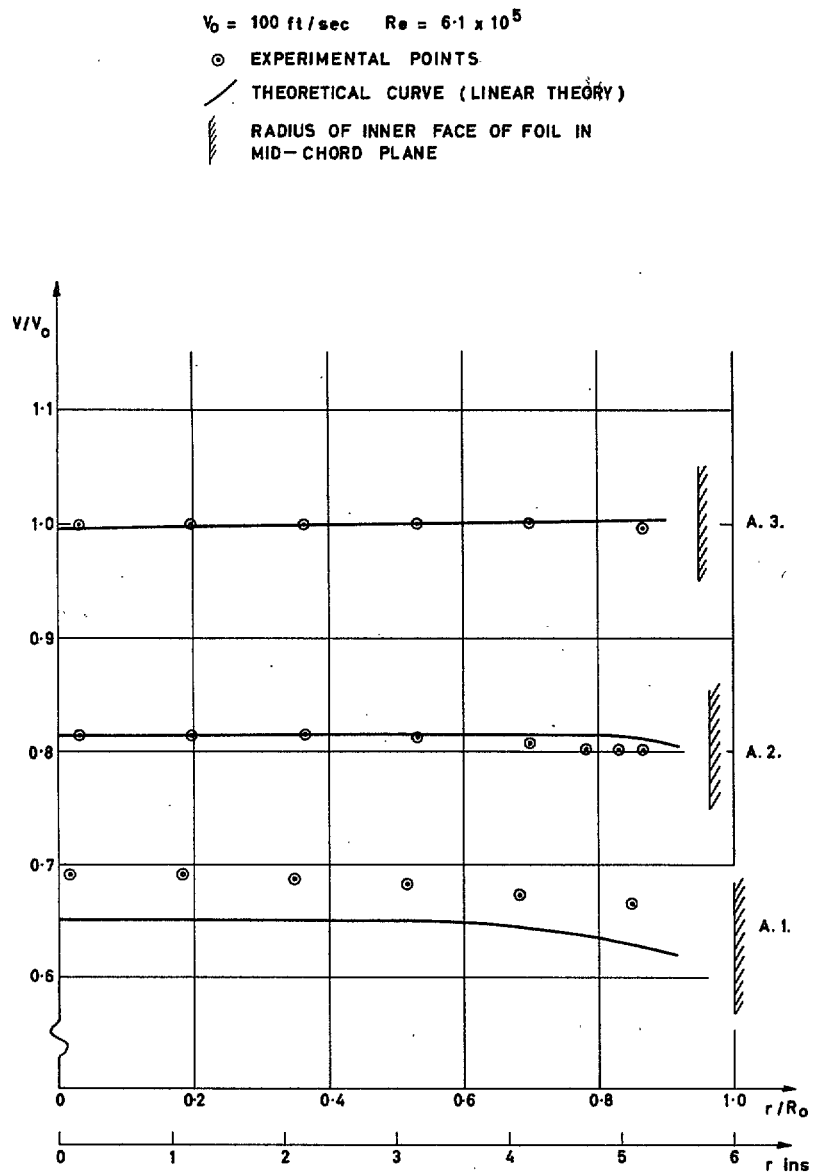

FIG. 12. Axial velocity distributions in mid plane of foils in design condition – Set A.

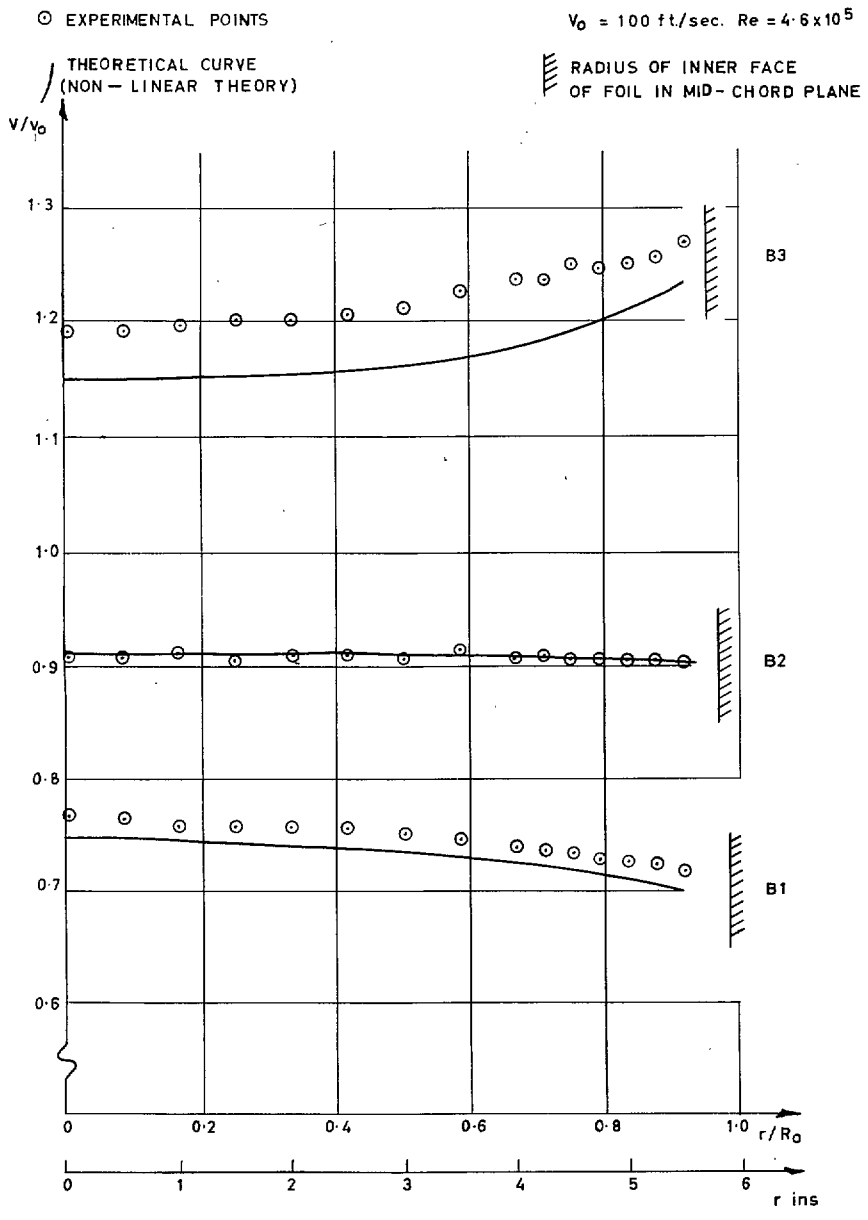

FIG. 13. Axial velocity distributions in mid plane of foils in design condition – Set B.

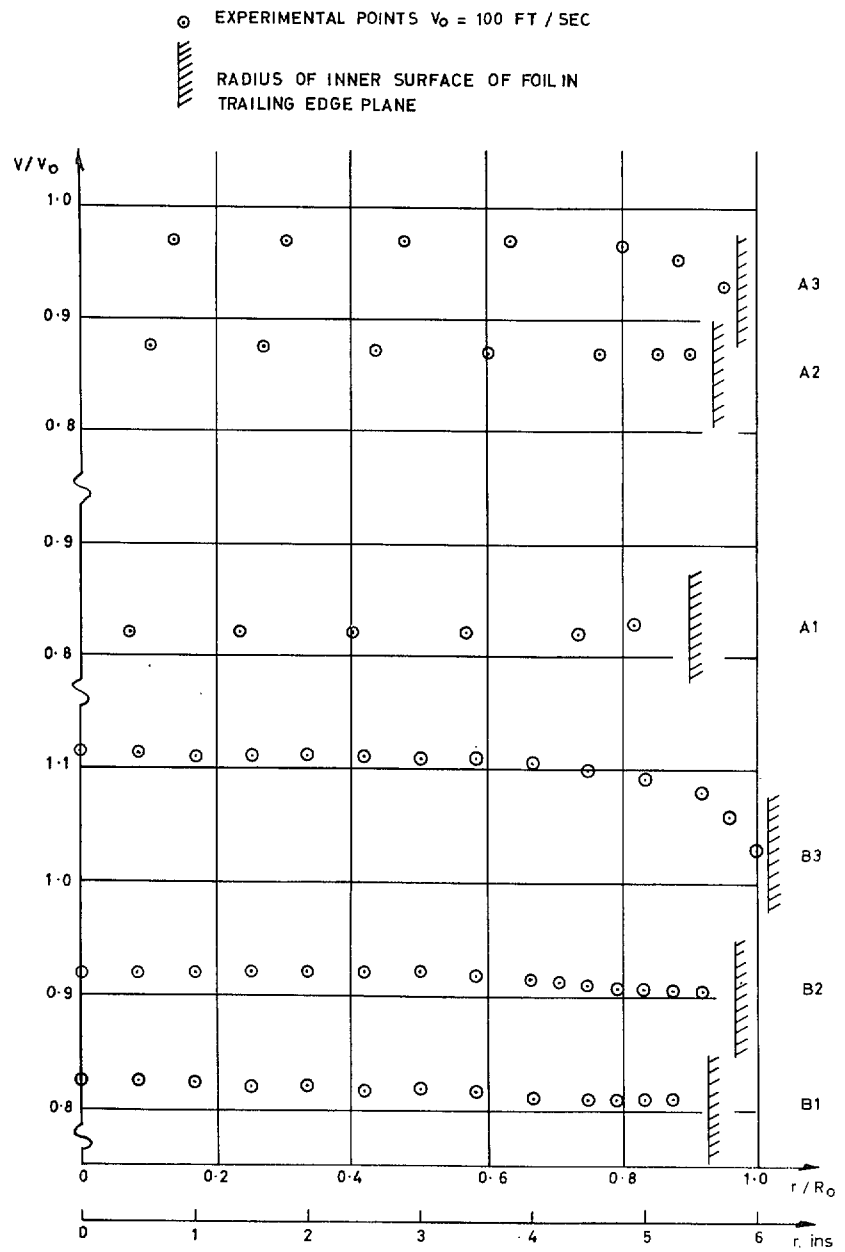

FIG. 14. Axial velocity distributions in trailing-edge plane of foils in design condition.

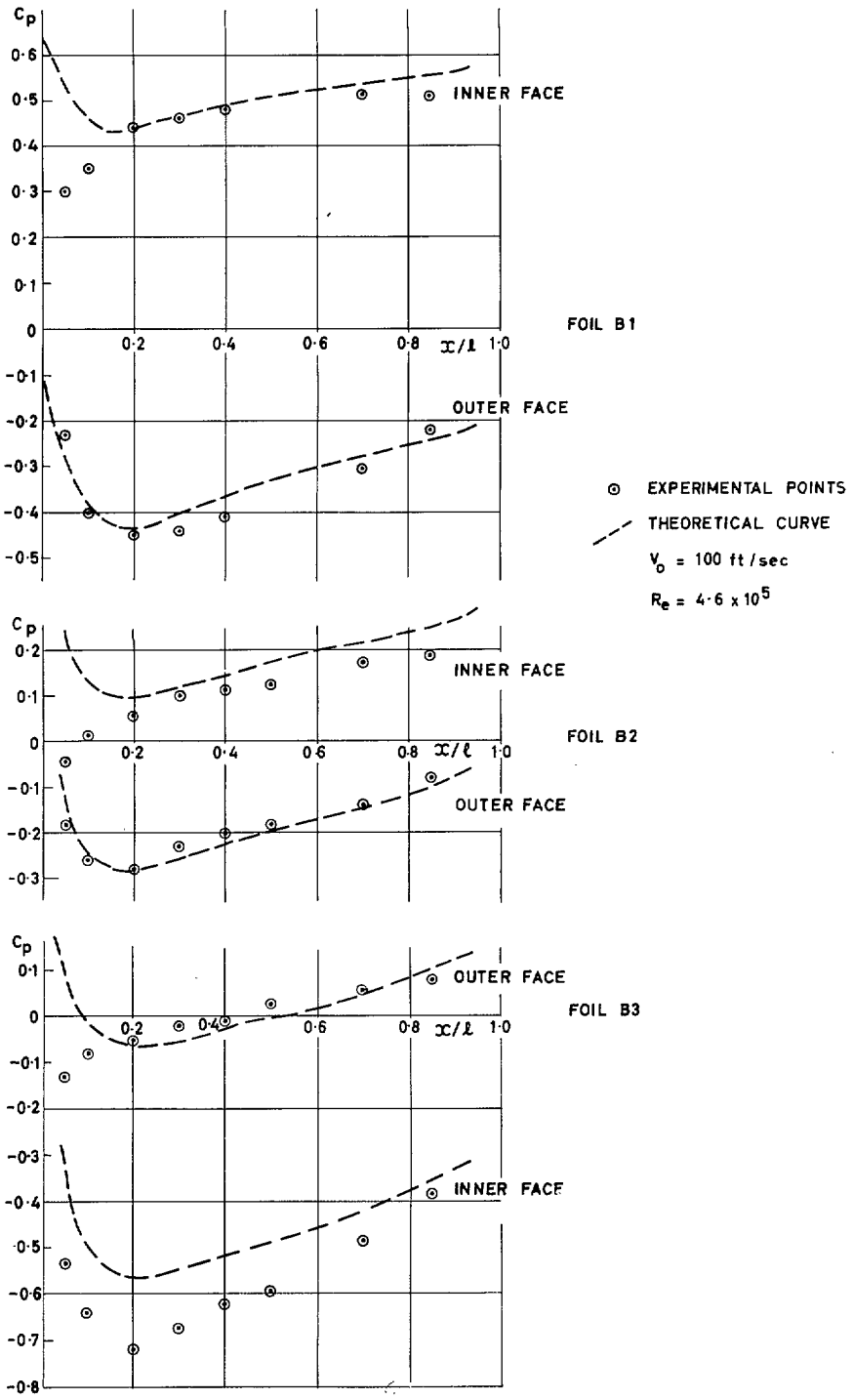

FIG. 15. Pressure distributions on foils of Set B at zero incidence.

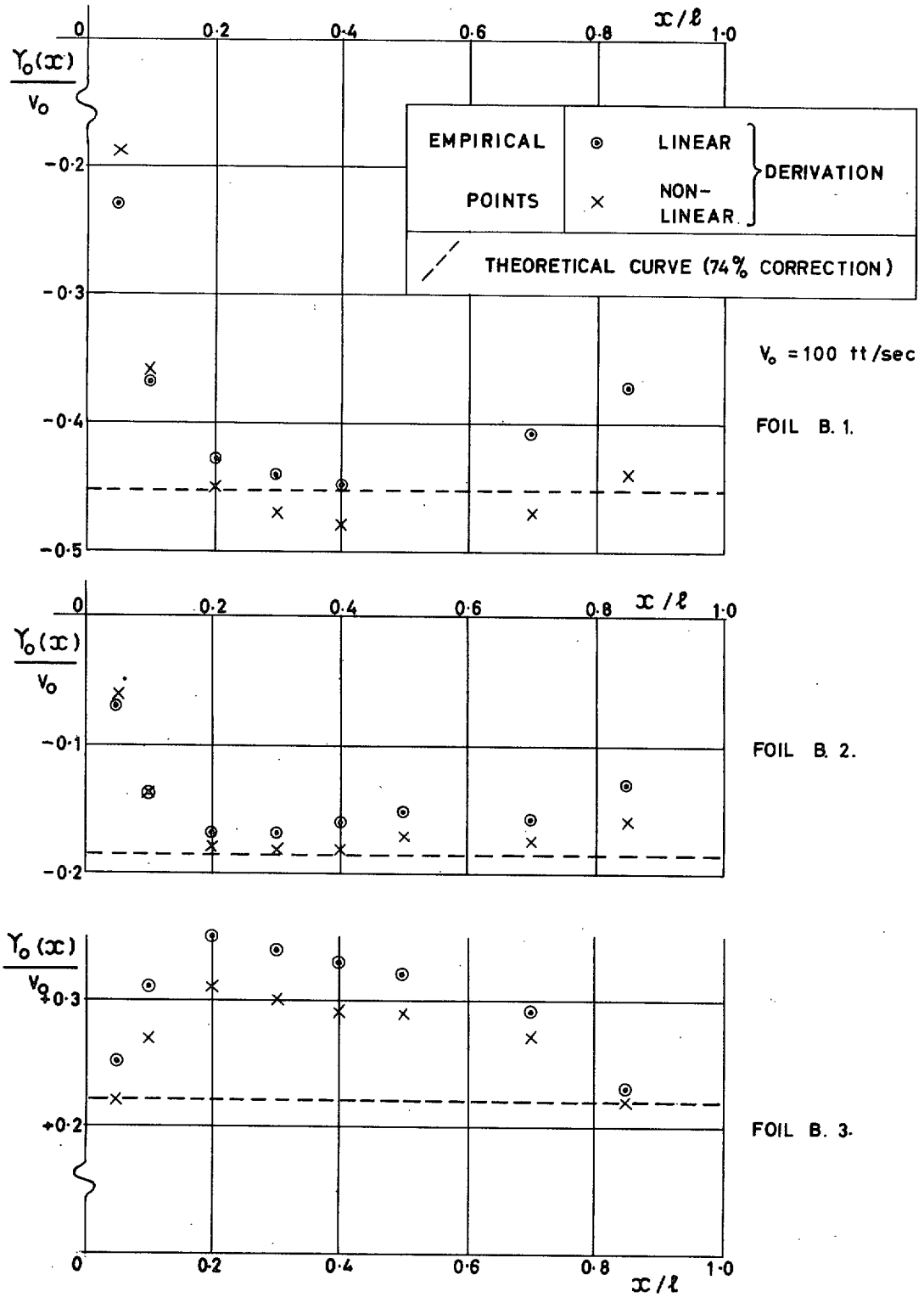

FIG. 16. Comparison of theoretical and empirical circulation distributions on foils – Set B.

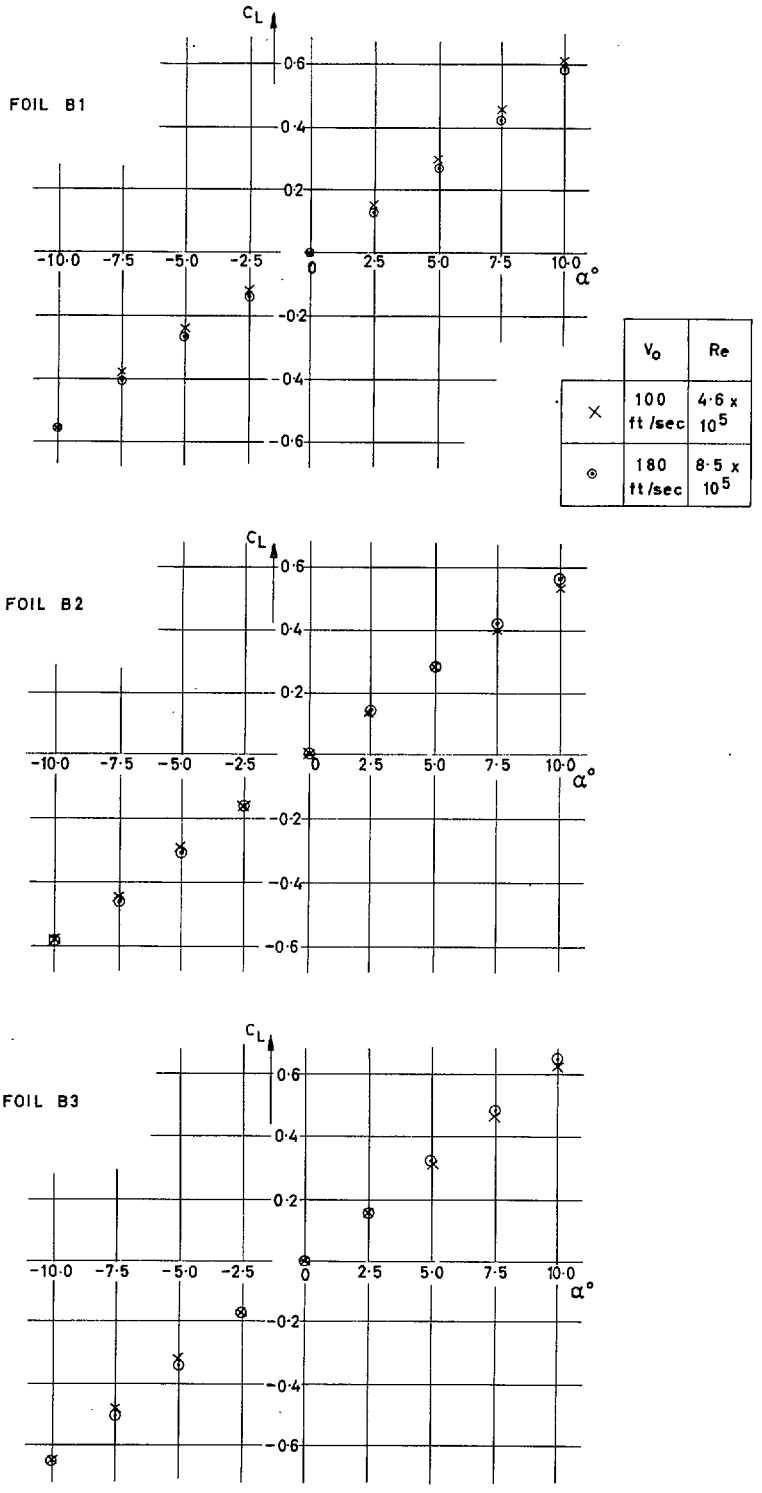

FIG. 17. Plot of lift coefficient against incidence.

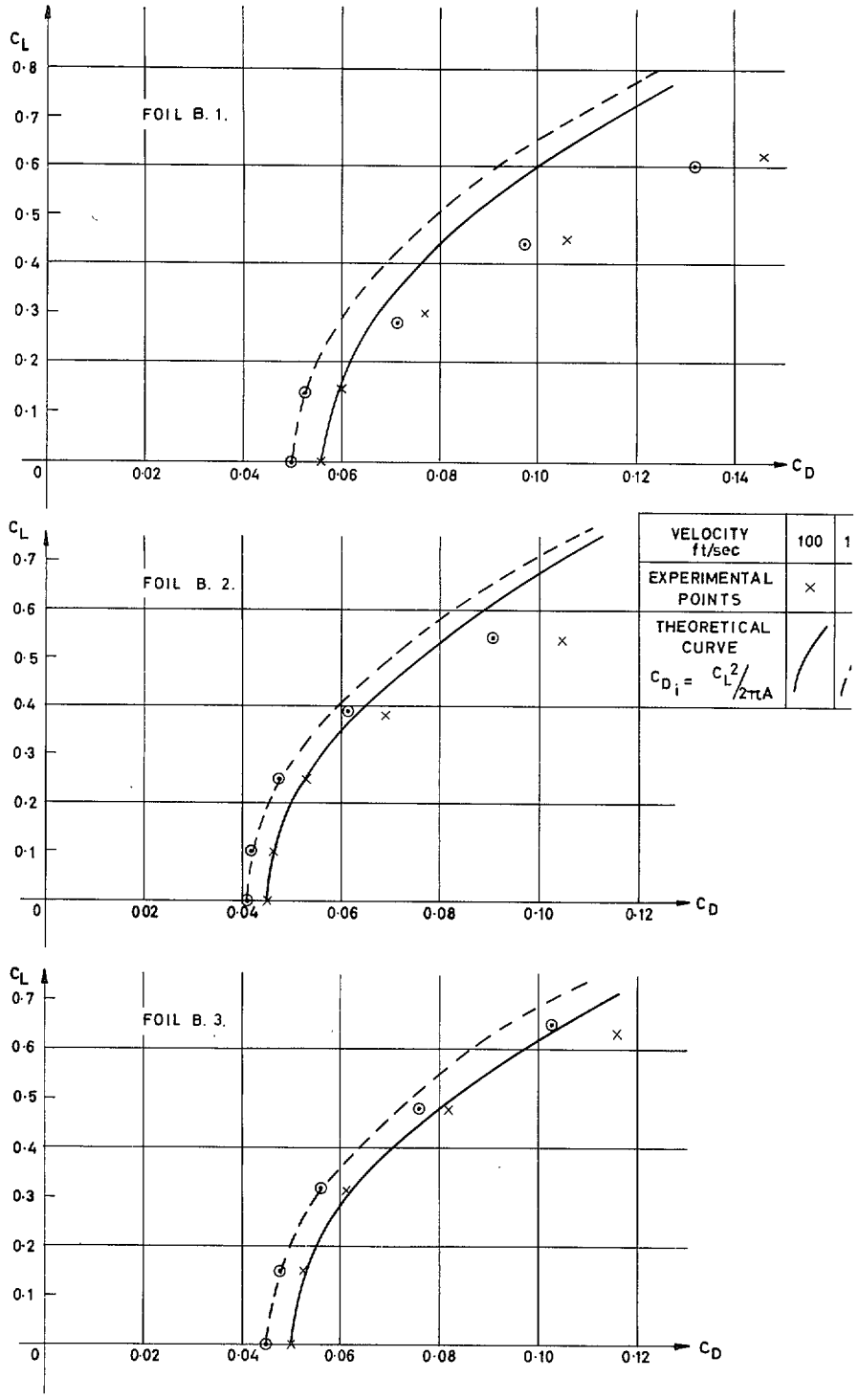

FIG. 18. Lift-drag polars for foils of Set B at incidence.

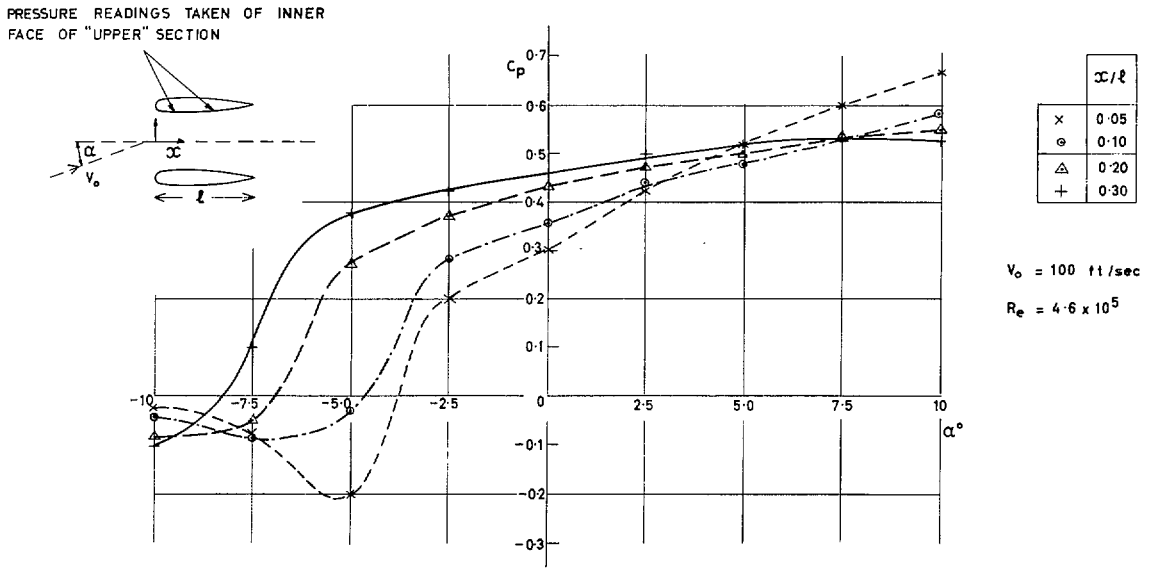

FIG. 19. Variation with incidence of the pressure coefficient at different chordwise stations – Foil B.1.

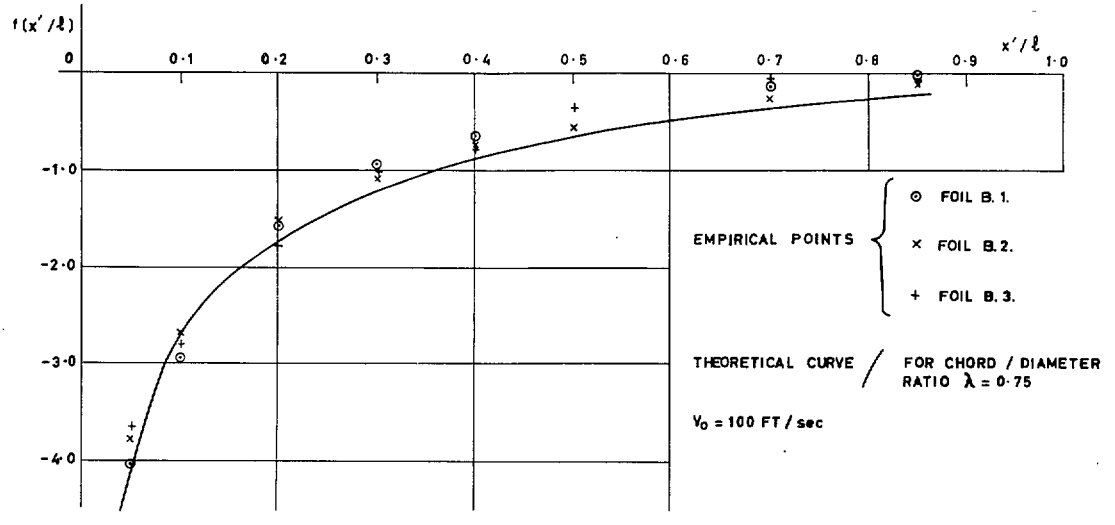

FIG. 20. Circulation loading due to incidence (values of $f(x'/l)$ evaluated from readings at ± 5 deg incidence).

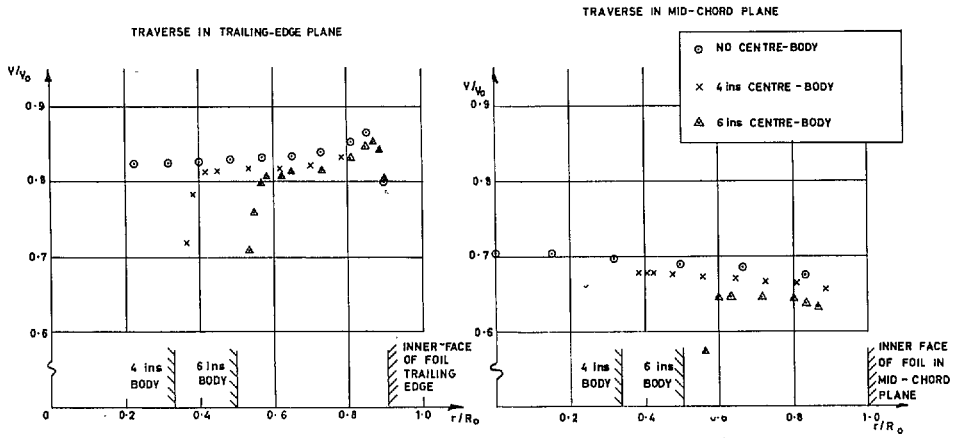

FIG. 21. Velocity traverses; annular aerofoils with concentric centre-body, Foil A.1. (V_0 = 180 ft./sec.).

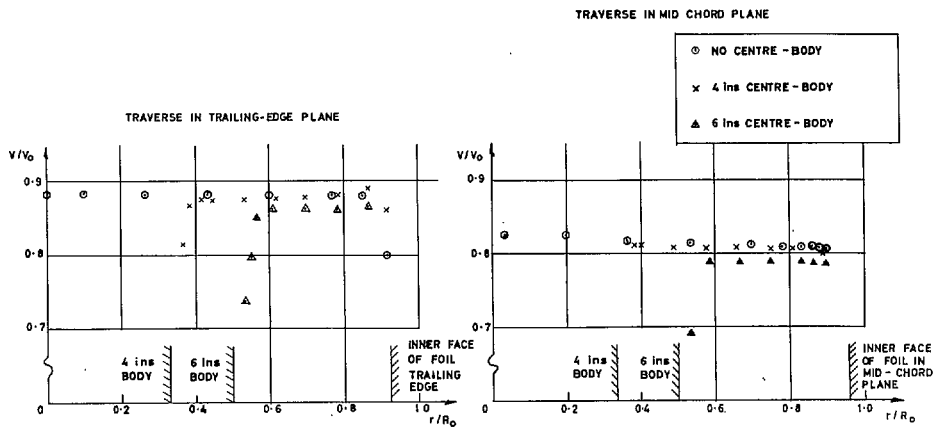

FIG. 22. Velocity traverses: annular aerofoils with concentric centre-body, Foil A.2. (V_0 = 180 ft./sec.).

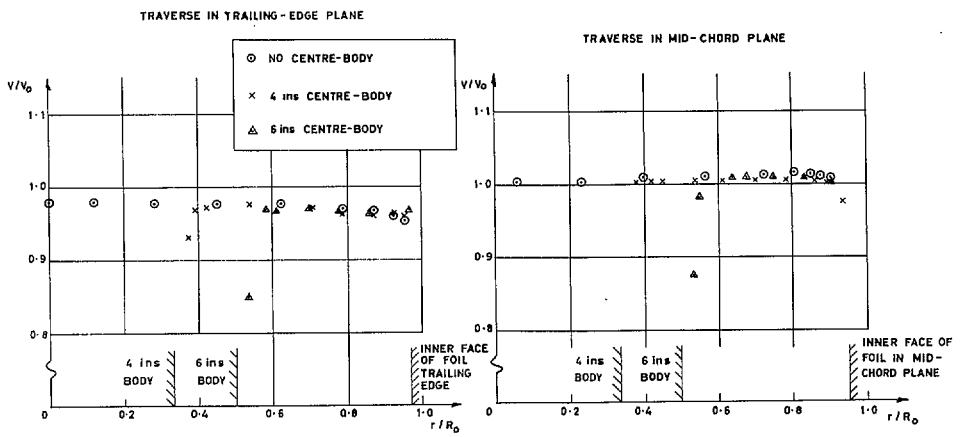

FIG. 23. Velocity traverses: annular aerofoils with concentric centre-body, Foil A.3. (V_0 = 180 ft./sec.).

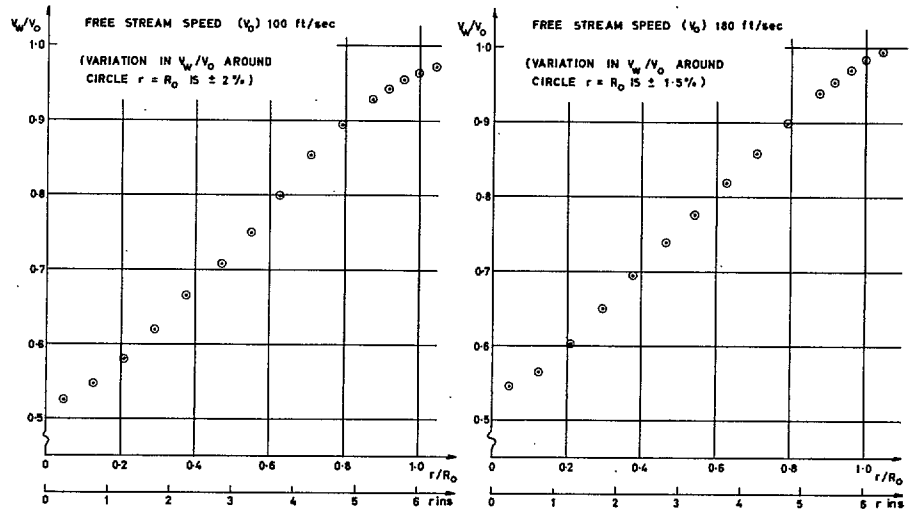

FIG. 24. Velocity traverses in wake of body.

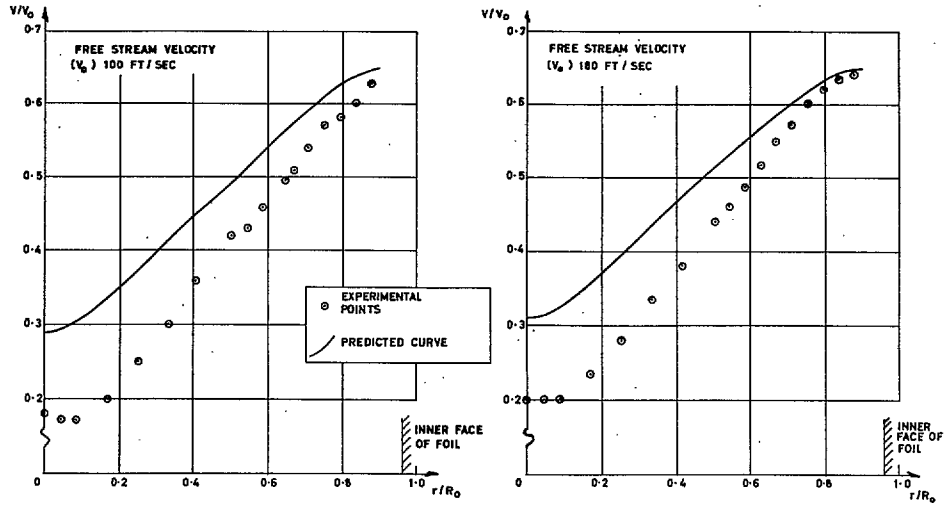

FIG. 25. Velocity traverse mid-chord plane of Foil, with wake inflow – Foil B.1.

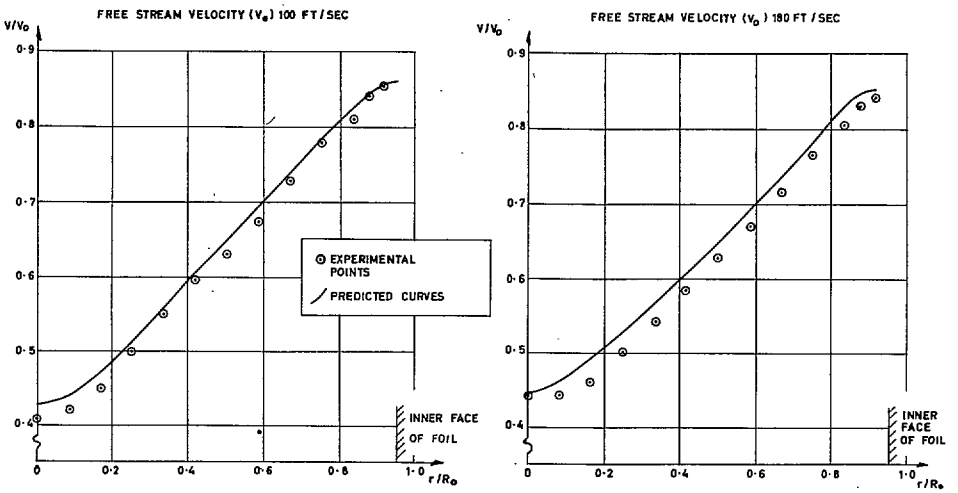

FIG. 26. Velocity traverse in mid-chord plane of Foil with wake inflow – Foil B.2.

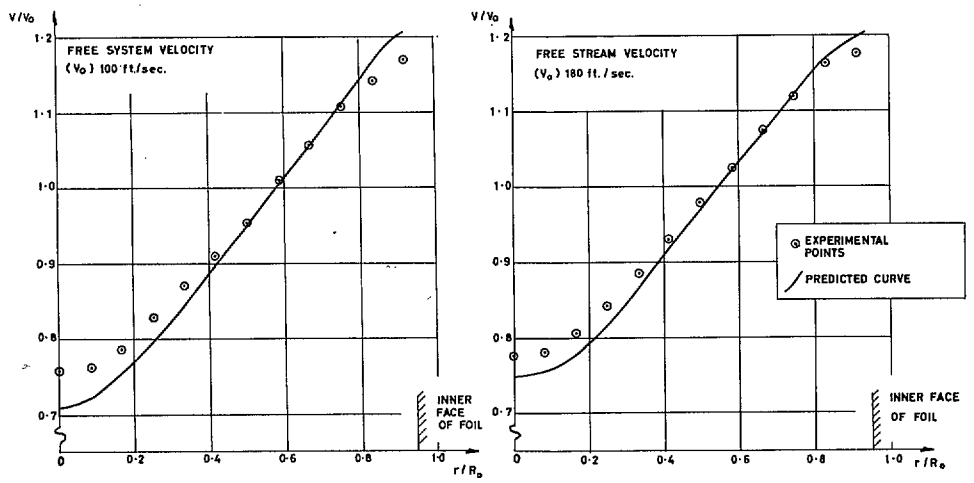

FIG. 27. Velocity traverse in mid-chord plane of Foil, with wake inflow – Foil B.3.

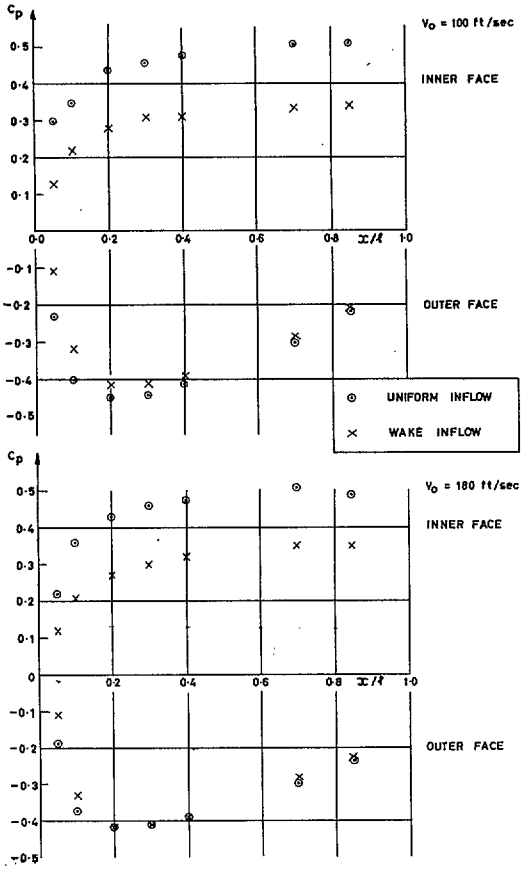

FIG. 28. Comparison of pressure distributions on Foils in uniform and wake inflow – Foil B.1.

Dd.129527 K5

Printed in Wales for Her Majesty's Stationery Office
by Allens Printers (Wales) Limited

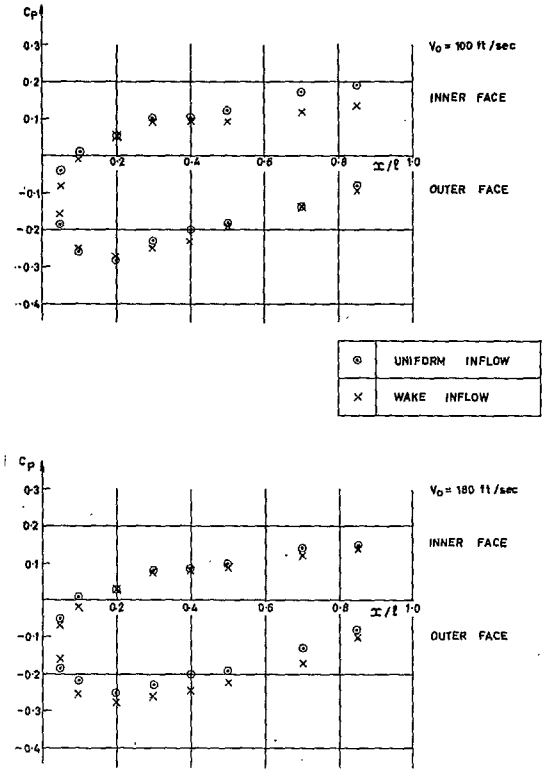

FIG. 29. Comparison of pressure distributions on Foils in uniform and wake inflow – Foil B.2.

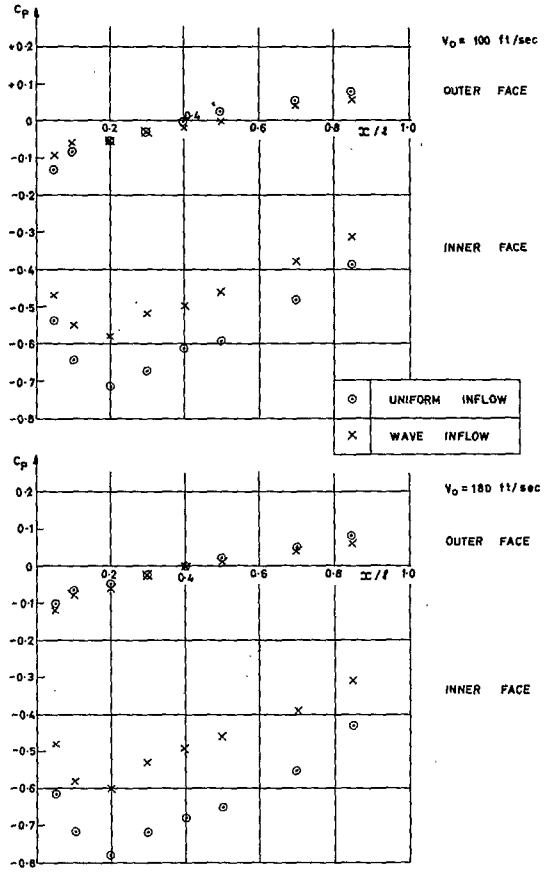

FIG. 30. Comparison of pressure distributions on Foils in uniform and wake inflow – Foil B.3.

Published by
HER MAJESTY'S STATIONERY OFFICE

To be purchased from
49 High Holborn, London W.C.1
423 Oxford Street, London W.1
13A Castle Street, Edinburgh 2
109 St. Mary Street, Cardiff
Brazennose Street, Manchester 2
50 Fairfax Street, Bristol 1
35 Smallbrook, Ringway, Birmingham 5
7–11 Linenhall Street, Belfast 2
or through any bookseller

S.O. Code No. 23–3492